Brainstem control of vocalization and its coordination with respiration

Citation: Park, Jaehong, Choi, Seonmi, Takatoh, Jun, Zhao, Shengli, Harrahill, Andrew et al. 2024. "Brainstem control of vocalization and its coordination with respiration." Science.

Published Version:

Publisher: American Association for the Advancement of Science

Permanent Link: https://hdl.handle.net/1721.1/153639

Version: Author's final manuscript: final author's manuscript post peer review, without publisher's formatting or copy editing

Brainstem control of vocalization and its coordination with respiration

Jaehong Park[1,2*], Seonmi Choi[1], Jun Takatoh[1], Shengli Zhao[3], Andrew Harrahill[1], Bao-Xia Han[3], Fan Wang[1*]

1. Department of Brain and Cognitive Sciences, McGovern Institute for Brain Research, Massachusetts Institute of Technology, Cambridge, MA 02139, USA
2. Department of Biomedical Engineering, Duke University, Durham, NC, 27708, USA
3. Department of Neurobiology, Duke University Medical Center, Durham, NC, 27710, USA

* Corresponding author. Email: fan_wang@mit.edu or jaehong@mit.edu

Phonation critically depends on precise controls of laryngeal muscles in coordination with ongoing respiration. However, the neural mechanisms governing these processes remain unclear. We identified excitatory vocalization-specific laryngeal premotor neurons located in the retroambiguus nucleus ($\mathrm{RAm}^{\mathrm{VOC}}$) in adult mice as both necessary and sufficient for driving vocal-cord closure and eliciting mouse ultrasonic vocalizations (USVs). The duration of $\mathrm{RAm}^{\mathrm{VOC}}$-activation can determine the lengths of both USV syllables and concurrent expiration periods, with the impact of $\mathrm{RAm}^{\mathrm{VOC}}$-activation depending on respiration phases. $\mathrm{RAm}^{\mathrm{VOC}}$-neurons receive inhibition from the preBötzinger complex, and inspiration-needs override $\mathrm{RAm}^{\mathrm{VOC}}$-mediated-vocal-cord closure. Ablating inhibitory synapses in $\mathrm{RAm}^{\mathrm{VOC}}$-neurons compromised this inspiration gating of laryngeal adduction, resulting in discoordination of vocalization with respiration. Our study revealed the circuits for vocal production and vocal-respiratory coordination.

One-Sentence Summary:

Identification of $\mathrm{RAm}^{\mathrm{VOC}}$-neurons as the critical node for vocal production and vocal-respiratory coordination.

Vocalization plays essential roles in communication in many species (*1, 2*). While the complexity of vocalization (i.e. articulation) varies depending on species, the fundamental sound production process (i.e. phonation) shares similarities. Phonation process dominantly occurs during expiration: narrowing of the larynx (vocal cord adduction) while simultaneously exhaling air (*3*). In general, phonations do not happen during inhalation because inspiration requires opening of the larynx (vocal cord abduction) (*4*). Furthermore, the need for inspiration suppresses vocalization (breathing primacy), as everyday experience illustrates that we have to stop talking when we need to breathe. Inappropriate adduction or abduction of the larynx in the wrong respiration phases can lead to inspiration problems or hoarse vocalizations (*5, 6*). However, the neural circuits that seamlessly coordinate laryngeal movements with respiration to produce phonations and to prioritize breathing needs have yet to be clearly delineated.

We reasoned that the key to answer this question is to first identify the neurons that drive laryngeal adduction for vocalization, followed by determining their interaction with respiratory circuits. The hindbrain contains premotor neurons that can activate laryngeal adductor motoneurons (*1, 2, 7*). The nucleus retroambiguus (RAm) located in the caudal-ventral brainstem is one key node for vocal production. Vocalizations induced by electrical stimulation of the midbrain periaqueductal gray (PAG) in decerebrate cats (*8, 9*) and anesthetized rats (*10*) are suppressed by lesions of the RAm. Pharmacological and electrical stimulation of the RAm evokes elementary sounds (*9-11*), although such sounds do not resemble species-typical vocalizations. The RAm region has vocalization-related neural activity (*12*), and shows a positive correlation between unit activity and vocal loudness (*13*). Neural tracers injected in the RAm labels axonal projections to the nucleus ambiguus (NA) where laryngeal motoneurons are located (*14*). However, the RAm region does not have anatomical demarcations and contains heterogeneous types of neurons including neurons modulating respirations and other orofacial movements (*15*). Thus, it remains unknown which populations in the RAm are vocalization-specific laryngeal premotor neurons and whether they are necessary and sufficient to drive vocal cord adduction and phonation, and if so, how these neurons interact with respiratory circuit to ensure vocal-respiration coordination and breathing primacy. With regard to respiration, intensive studies have been conducted on the inspiration rhythm generator, the preBötzinger complex (preBötC) (*16-19*). However, only one study investigated the function of the preBötC during vocalizations in awake animals (*20*). As such, it is still unclear how inspiration gates the activity of hindbrain vocal production circuits.

We used mouse ultrasonic vocalization (USV) as a model system. During interactions with female mice, male mice readily emit USVs comprising a string of syllables periodically interrupted by inspiration, also called courtship songs (*21, 22*). Unlike audible vocalizations, which are produced by air vibrating the tightly-closed vocal cords (*23*), USVs are produced by a whistle-like mechanism: a jet stream of air coming through a small hole formed between the adducted vocal cords (*24-26*), thereby generating pure-tone sounds in ultrasonic frequency range. Despite the unique phonation mechanism, USVs still require laryngeal adduction and necessitate the adduction occurring during expiration (*24*), thereby providing us a suitable model for vocal-respiratory coordination.

Vocalization-specific laryngeal premotor neurons in the brainstem

The activity of laryngeal muscles and motoneurons is controlled by premotor neurons in the hindbrain (*1, 7*). However, the location and identity of the vocal premotor circuits in *adult* mammals have yet to be revealed. We applied three-step monosynaptic rabies virus tracing (*27*) (Fig. 1A), combining AAVretro-Cre (injected into laryngeal muscles in juvenile animals), Cre-dependent helper AAVs (to express TVA receptor and optimized rabies glycoprotein (oG) in motoneurons), and pseudo-typed G-deleted rabies virus (EnvA^{M21}-RV-GFP, injected into the NA in adults). Cre^{+} motoneurons were found around the NA (Fig. 1B), and trans-synaptically labeled laryngeal premotor neurons were mostly observed in the brainstem (Fig. 1C), specifically in the Kölliker-Fuse (KF), parvocellular reticular formation (PCRt), lateral paragigantocellular nucleus (LPGi), intermediate reticular nucleus (IRt), preBötC, nucleus tractus solitarii (NTS), and RAm. We registered all labeled neurons in the Allen common coordinate frame for the mouse brain (Allen CCF) (*28*) and compared the map of laryngeal premotor neurons to our previously identified maps of jaw and tongue premotor neurons (*27*) (fig. S1). The overall spatial distributions of laryngeal premotor neurons from different mice (n=3) were similar, but they were distinct from those of jaw and tongue premotor maps (fig. S1). Labeled premotor neurons also had extensive collateral projections to other branchial motor nuclei, including the trigeminal (5N), the facial (7N), and the hypoglossal (12N) nuclei (fig. S1), suggesting that laryngeal premotor neurons might simultaneously recruit other orofacial motoneurons for vocalization and perhaps for other orofacial movements.

Previous studies have suggested that the RAm is a critical node for vocal production (*7, 14*). When we examined *Fos* mRNA expression (a marker for activated neurons) in male mice 90 min after female-induced courtship USVs (Fig. 1D), we detected robust *Fos* signals in the RAm (fig. S2). By contrast, fewer and weaker *Fos* expressions were found in other hindbrain areas, such as the preBötC in the same samples (fig. S2). Our laryngeal premotor tracing consistently labeled a cluster of RAm neurons (Fig. 1C). We further confirmed that the majority of rabies-traced laryngeal premotor neurons in the RAm induced Fos expression after bouts of courtship USVs (68.6±13.1 %, GFP+ and Fos+ neurons/GFP+ neurons, n=4 mice, Fig. 1E).

We used the Fos-based cell targeting method called CANE (*29*) to label courtship USV-activated RAm neurons in male mice (RAm^{VOC}-neurons) (Fig. 2A). After expressing GFP in RAm^{VOC}-neurons via CANE, we re-exposed male mice to females to re-elicit USVs and Fos expression and confirmed that labeled RAm^{VOC} were indeed Fos+ (Fig. 2B). We further registered the locations of all CANE-captured RAm^{VOC}-neurons in the Allen CCF and confirmed that their positions overlapped with those of the rabies-traced RAm laryngeal premotor neurons (Fig. 2C). We further examined the expression of ChAT, a molecular marker for motoneurons, and found that none of the labeled RAm^{VOC}-neurons expressed ChAT (Fig. 2D), i.e., CANE did not capture cholinergic motoneurons. Furthermore, the axonal boutons from RAm^{VOC}-GFP cells innervated ChAT positive motoneurons around the NA (Fig. 2D), consistent with them being vocal premotor neurons. Lastly, in-situ hybridization using *Vglut2* and *Vgat* probes showed that majority of RAm^{VOC}-neurons were glutamatergic (*Vglut2*+/RAm^{VOC}: 85.1±0.1%, *Vgat*+/RAm^{VOC}: 12.9±0.1%, n=3 mice, Fig. 2E), suggesting that they provide excitatory inputs to laryngeal motoneurons.

Silencing RAm^{VOC}-neurons abolishes both ultrasonic and audible vocalizations

To dissect the functional role of RAm^{VOC}-neurons, we bilaterally expressed tetanus toxin light chain (TeLC) to inhibit their synaptic outputs (*30*) or expressed GFP as controls using CANE (Fig. 2F). RAm^{VOC}-GFP male mice emitted robust USVs in the presence of female mice before and after CANE-mediated expression (Fig. 2G upper and H left). In contrast, RAm^{VOC}-TeLC mice failed to vocalize in response to female mice after TeLC expression (Fig. 2G bottom and H right).

The effect of silencing RAm^{VOC}-neurons was robust and consistent: all six RAm^{VOC}-TeLC mice had complete mutism during courtship (Fig. 2I).

In addition to social USVs, mice also elicit audible squeaks in response to strongly aversive stimuli (*31*). Prior studies suggested that USVs and squeaks are triggered by different neural pathways (*31, 32*). For example, a recent study showed that inhibition of the PAG-RAm pathway only abolished USVs but not pain-elicited audible vocalizations (*32*). We evoked squeaks in mice using a tail-pinch stimulus (Fig. 2J). While control RAm^{VOC}-GFP mice responded with robust cries, RAm^{VOC}-TeLC mice were silent (Fig. 2K and L). Furthermore, when we applied foot-shocks, RAm^{VOC}-GFP (Movie S1), but not RAm^{VOC}-TeLC mice (Movie S2), squeaked, even though all mice exhibited escape behaviors, indicating that nociceptive responses of the RAm^{VOC}-TeLC mice were intact.

To rule out the possibility that mutism in the RAm^{VOC}-TeLC mice originated from general breathing abnormalities, we habituated mice on a treadmill wheel and gently encouraged them to run (fig. S3). Running changes both the frequency and amplitude of breathing in mice (*33*). The modulation of respiration by running in RAm^{VOC}-TeLC mice remained intact as that in the control group (RAm^{VOC}-TeLC (n=3) vs RAm^{VOC}-GFP (n=4). Changes in inspiratory amplitude: 27.8±8.4% vs 24.4±2.6%, p=0.8597; expiratory amplitude: 12.6±6.6% vs 6.5±1.1%, p=0.5959; frequency: 36.7±18.3% vs 27.3±9.5%, p=0.5959, Mann-Whitney U test, fig. S3).

We also observed some axon collaterals of RAm^{VOC}-neurons in the thoracic spinal cord segment (fig. S4), where abdominal spinal motor neurons for active expiration are located, suggesting that RAm^{VOC} might be involved in increasing expiratory activity needed for generating sound (phonation). To test this idea, we measured abdominal EMG of anesthetized RAm^{VOC}-TeLC mice during PAG stimulation-induced vocalizations (fig. S4). A previous study has shown that optogenetic stimulation of RAm-projecting PAG neurons (PAG^{RAm}) could reliably elicit USVs in mice (*32*). PAG^{RAm} neurons were labeled by injecting AAVretro-FlpO in the RAm, and injecting Flp-dependent optogenetic activator ChRmine (*34*) in the PAG, and in the same male mouse, RAm^{VOC} neurons were targeted to express either GFP or TeLC using CANE (fig. S4). While PAG^{RAm} stimulation reliably elicited abdominal EMG activity concurrent with USVs in the GFP control mice, the same stimulation failed to elicit USVs and abdominal EMG responses in the TeLC mice (fig. S4).

RAm^{VOC}-activation is sufficient to elicit and modulate USVs in mice

In addition to active expiration, vocal production critically depends on vocal cord adduction. The nearly closed larynx is essential for the exhaling jet stream of air to whistle USVs, or to vibrate the vocal cords to produce audible sounds (*24-26*). To determine whether RAm^{VOC}-neurons are sufficient to close the vocal cords and elicit USVs, we expressed ChRmine (*34*) in these neurons using CANE in male mice (Fig. 3A). First, the larynx was imaged with a camera while mice were anesthetized and placed in a prone position (Fig. 3B). The vocal cords naturally widened and narrowed (but not fully closed) rhythmically (Fig. 3C, Movie S3), in phase with inhalation and exhalation, resulting in periodic changes in the size of the glottal area (Fig. 3D). Optogenetic activation of RAm^{VOC} with 5s continuous laser illumination instantaneously closed the vocal cords, and the laryngeal adduction persisted throughout the stimulation (Fig. 3D, n=3 mice, Movie S3). This prolonged laryngeal adduction was interrupted by occasional glottal openings during the 5s stimulation in all mice tested (this point is further elaborated below). We next stimulated RAm^{VOC} in awake male mice to check whether this was sufficient to elicit USVs

(Fig. 3E). Applying a brief 100ms laser pulse reliably induced USVs time-locked to each pulse (Fig. 3F). The onset latencies of the optogenetic-induced ultrasonic vocalizations were short (39.0.0±1.1ms, Fig. 3G). All RAm^{VOC}-activation-elicited vocalizations were in ultrasonic range (RAm^{VOC}-USV), and the syllable patterns of RAm^{VOC}-USVs included several typical types of female-directed USVs (*35*) (up, step-down, chevron, two-steps, short, but also unstructured ones, Fig. 3H). We also compared RAm^{VOC}-USVs and female-directed USVs for several acoustic features, and observed similar distributions for loudness, spectral purity, and pitch variance (Fig. 3I). Note that the mean frequency of the RAm^{VOC}-USVs was different, i.e., lower than that of the female-directed USVs in the same mice (RAm^{VOC}-USVs: 61.8±0.4 kHz, female-directed: 79.6±0.2 kHz, $p \leq 0.0001$, Mann-Whitney U test), indicating other neurons are needed for producing the full frequency range of natural USVs.

Given that a brief RAm^{VOC}-activation elicited a single short USV syllable (Fig. 3F), we also tested whether RAm^{VOC}-activation can alter the length of individual USV syllables. We varied the duration of optogenetic stimulation of RAm^{VOC} (50, 100, and 200ms), and observed that indeed the length of RAm^{VOC}-USV syllables were proportionally correlated to the duration of laser stimuli (Fig. 4B and D).

Vocalization-respiration coordination during RAm^{VOC} activation

For normal vocalization, sound is exclusively produced during the expiration phase (*4*). The results described above highlighted the role of RAm^{VOC}-neurons in driving laryngeal adduction while coordinating expiration efforts. However, inspiration-needs must be prioritized (breathing primacy) to ensure survival. To investigate the precise role of RAm^{VOC} in vocal-respiration coordination, we simultaneously measured USVs and respiratory activity in awake mice while optogenetically stimulating RAm^{VOC} with different durations (50, 100, and 200ms) (Fig. 4A-C). Longer RAm^{VOC}-activation induced longer duration of expiration characterized by a flat period on the respiratory traces (Fig. 4C and E). The durations of RAm^{VOC}-induced-USVs and flat expirations were highly correlated (R^2=0.922), consistent with the notion that RAm^{VOC}-activity coordinately mediates vocal cord closure and expiration.

We next asked whether the impact of RAm^{VOC}-activation is dependent on the current on-going respiratory phases. To test this idea, we analyzed the latencies and durations of RAm^{VOC}-induced flat expirations and USV syllables with respect to the onsets of laser RAm^{VOC}-activation in respiration phases (F_{laser}, Fig. 4F). Interestingly, RAm^{VOC}-stimulation at the early expiration (F_{laser} during 0 to 0.5π) and late inspiration phases (F_{laser} during -0.5π to 0) produced longer durations of expirations and USVs with short latencies, while RAm^{VOC}-activation in the late expiration (F_{laser} during 0.5π to π) and early inspiration phases (F_{laser} during -π to -0.5π) elicited shorter expirations and shorter USVs with longer latencies (Fig. 4 G and H).

With 200ms of RAm^{VOC}-activation, we occasionally observed a full inspiration cycle during stimulation (200ms, Fig. 4C). Similarly, in the anesthetized larynx imaging preparation, the vocal cords were occasionally open during prolonged 5s RAm^{VOC}-activation, presumably due to an “override” by the need for inspiration (Fig. 3D). To further investigate this inspiratory gating of vocalization/vocal adduction in awake mice, we applied 2s continuous RAm^{VOC}-activation. This 2s stimulation produced multiple USV syllables accompanied by concurrent flat expiration periods, which were periodically interrupted by intervening inspirations (Fig. 4I). The amplitudes of the intervening inspirations were similar to those in the baseline conditions, indicating that these are normal breaths (Fig. 4I). We projected the onsets and offsets of the multiple USV syllables evoked by the 2s RAm^{VOC}-activation onto respiration phase maps (Inspiration: -π to 0, Expiration: 0 to π, Fig. 4J). All syllables were exclusively found in the expiration phase (Fig. 4K), consistent with the notion that intervening inspirations can stop the on-going USVs evoked by RAm^{VOC}-activation, i.e., inspiration gates and sets the basic rhythm of vocalization.

Inhibitory inputs to RAm^{VOC} are essential for inspiration gating of vocalizations

We hypothesized that inhibitory inputs onto RAm^{VOC}-neurons are the key for the periodic suppression of vocalization by inspiration. To identify the source of inspiration-related inhibitory inputs to the RAm^{VOC}-neurons, we performed monosynaptic tracing of presynaptic neurons to RAm^{VOC} (preRAm^{VOC}). This was achieved by expressing TVA and oG in RAm^{VOC} using CANE, followed by infecting these neurons with EnvA^{M21}-RV-GFP (Fig. 5A). Tracing results showed that RAm^{VOC}-neurons receive excitatory inputs from the PAG, the parabrachial (PB)/KF, and other areas (Fig. 5B). Excitatory PAG neurons are known to be required for eliciting USVs but not for generating rhythmic vocal patterns (*32*). The dominant source of inhibitory inputs to RAm^{VOC}-neurons was the preBötC (Fig. 5B), the inspiration rhythm generator (*19*). In our mapping of laryngeal premotor neurons, we also labeled a population of inhibitory neurons in the preBötC (fig. S5). Thus, the preBötC provides inhibitory inputs to both vocal motoneurons (MN^{VOC}) and to RAm^{VOC} (Fig. 5C), consistent with a recent axonal tracing study of inhibitory preBötC neurons (*36*). These results suggest that the inspiration-controlled periodic patterns of USVs could be generated by tonic excitatory inputs from the PAG to RAm^{VOC} to induce vocal cord adduction (and concurrent expiration), which is gated by rhythmic inhibition from the preBötC to both MN^{VOC} and RAm^{VOC} (Fig. 5C).

To validate the functional relevance of the anatomical connections identified above, we decided to block inhibitory inputs to RAm^{VOC}-neurons. Based on the circuit diagram, we predicted that disinhibited RAm^{VOC} would provide stronger and tonic excitatory drive to MN^{VOC}, that counters the rhythmic inhibitory drive from the preBötC, such that vocal cord adduction may happen even during inspiration. Furthermore, if the activity of disinhibited RAm^{VOC} was sufficiently elevated, spontaneous vocalization (in the absence of social interactions) might occur. We expressed GFE3 in *glutamatergic* RAm^{VOC}-neurons using CANE (RAm^{VOC}-GFE3 mice), with RAm^{VOC}-GFP mice as control (Fig. 5D). This was achieved by injecting Cre-dependent CANE-hSyn-DIO-tTA together with AAV-TRE3G-GFE3 (or GFP) in the RAm in Fos^{TVA}/Vglut2-Cre double transgenic male mice after bouts of courtship USVs. GFE3 is a ubiquitin ligase specifically targeting the inhibitory post-synaptic scaffolding protein gephyrin for degradation (*37*), thereby reducing phasic synaptic inhibition onto RAm^{VOC}-neurons. To reliably elicit USVs in awake head-fixed mice, we again chose to perform optogenetic stimulation of RAm-projecting PAG neurons (PAG^{RAm}) (*32*). Briefly, in the same RAm^{VOC}-GFE3 or control mice, we also expressed ChRmine in RAm-projecting *Vglut2^{+}* PAG neurons (PAG$^{RAm/vglut2}$) using a Flp/Cre intersectional strategy (Fig. 5D). In control RAm^{VOC}-GFP mice, continuous pulses of optogenetic stimulation of PAG$^{RAm/vglut2}$ reliably elicited USVs but only during expirations, as the expirations were periodically interrupted by the inspiration flows (Fig. 5E-F upper panels). In addition, the peak flow values for the inspiration (downward trace) increased during the optogenetic PAG stimulation (123.1±6.1%, n=4 mice, Fig. 5E and G), suggesting PAG$^{RAm/vglut2}$ activation enhances inspiration (likely for inhaling sufficient air for vocalization). By contrast, in RAm^{VOC}-GFE3 mice, the inspiratory interruption of vocalization was severely compromised during continuous PAG$^{RAm/vglut2}$ activation (Fig. 5E, lower panels). The amplitude of the few intervening inspirations during PAG stimulations was significantly reduced compared to the average inspiration peak before stimulation (49.6±10.5%, n=5 mice, p=0.020, Mann-Whitney U test for GFE3 vs GFP mice, Fig. 5F and G, lower panels). We observed that asthma-like vocal sounds were produced during the inspiration periods in $\mathrm{RAm}^{\mathrm{VOC}}$-GFE3 (21.8±5.4%, n=5 mice, Fig. 5F, gray-shaded region, and 5G), while these abnormal inspiratory vocal sounds were never observed in the $\mathrm{RAm}^{\mathrm{VOC}}$-GFP control mice during $\mathrm{PAG}^{\mathrm{RAm/vglut2}}$ activation. Thus, removing inhibitory synaptic inputs to $\mathrm{RAm}^{\mathrm{VOC}}$-neurons compromises inspiration-gating of vocalization. The reduced inspiration amplitude is likely caused by persistent vocal cord adduction, due to a tonic excitatory drive from the disinhibited $\mathrm{RAm}^{\mathrm{VOC}}$. This persistent vocal cord adduction during inspiration could also explain the abnormal asthma-like inspiratory vocalizations. Finally, consistent with the idea that tonic activation of disinhibited $\mathrm{RAm}^{\mathrm{VOC}}$-neurons would cause spontaneous vocal cord closures, $\mathrm{RAm}^{\mathrm{VOC}}$-GFE3 mice also produced occasional spontaneous USVs in the absence of social contexts (0.5±0.2 VOC/s, n =6 mice, fig. S6), whereas control male mice almost never utter spontaneous USVs.

Discussion

We detected a vocalization-specific laryngeal premotor population in the RAm region of the caudal hindbrain ($\mathrm{RAm}^{\mathrm{VOC}}$) as the critical node for driving laryngeal adduction and phonation. We further uncovered neural mechanisms involving preBötC-$\mathrm{RAm}^{\mathrm{VOC}}$ interactions that ensure breathing primacy by allowing rhythmic inspirations to pace vocalizations. It has been debated whether the neural circuits for laryngeal adduction and vocal production are distributed across the ventral brainstem (*7*) or localized in one small area, such as the RAm (*14*). Here we found that inhibition of $\mathrm{RAm}^{\mathrm{VOC}}$-neurons not only abolished USVs in social contexts but also audible squeaks during aversive states (tail-pinch or foot-shock). Thus, $\mathrm{RAm}^{\mathrm{VOC}}$ represents a singular *necessary* locus for all phonations. On the other hand, optogenetic stimulation of $\mathrm{RAm}^{\mathrm{VOC}}$-neurons was sufficient to produce and *only* produced USVs, but not audible sounds. USVs and squeaks in rodents have different acoustic features. USVs lie above ultrasonic range (> 20kHz) with pure tones (*21, 22*), and rodents use aerodynamic mechanisms to produce USVs (*24-26*), while audible-squeaks occupy a human hearing frequency range (below 20kHz), with harmonics (*38*). Thus, squeaks likely require additional circuit elements, such as those driving strong air exhalation, which are not activated or recruited by $\mathrm{RAm}^{\mathrm{VOC}}$.

USVs can be further modulated in terms of frequency and duration. The duration of mouse vocalizations could be modulated by $\mathrm{RAm}^{\mathrm{VOC}}$-activity, but the mean frequency of $\mathrm{RAm}^{\mathrm{VOC}}$-USVs were lower than those of female-directed USVs in the same animals (Fig. 3). These data suggest that another parallel premotor pathway to laryngeal motor neurons (e.g., to vocal tensor muscles, such as cricothyroid muscles) might be involved in vocal frequency regulation. One potential frequency modulating region is the PCRt, which contains laryngeal premotor neurons as shown in our transsynaptic tracing study (Fig. 1C). This region, referred to as the vocalization-related parvicellular reticular formation (VoPaRt) in rats, is a node for high frequency vocalization (*10*). For duration modulation, we showed that optogenetically increasing the time of $\mathrm{RAm}^{\mathrm{VOC}}$-activation elongated the syllable length (Fig. 4B and D). Interestingly, transsynaptic tracing of pre-$\mathrm{RAm}^{\mathrm{VOC}}$ neurons labeled inputs in the PB/KF (Fig. 5B), which could be the endogenous region controlling $\mathrm{RAm}^{\mathrm{VOC}}$-activation and vocal duration based on previous pharmacological studies (*39*). However, the PB/KF regions are heterogeneous, including intermingled non-vocal respiratory neurons (*40, 41*), therefore future work targeting vocal-specific PB/KF will be needed to reveal the precise role of PB/KF in controlling vocal durations. Furthermore, it will be interesting to know whether and how the other recently identified brainstem vocal modulatory loci, the iRO in neonate mice (*42*) interacts with RAm^{VOC} to modulate other features of vocalizations.

Breathing is vital for survival. As breathing and vocalization both occur in the airway, laryngeal closure for sound production needs to be precisely controlled and coordinated with respiration. Failure in such coordination could lead to vocal cord dysfunction and breathing problems (*5, 6*). We found evidence of inspiration dominance over RAm^{VOC}-USVs: the effect of brief RAm^{VOC}-activation was delayed and attenuated around the onset of inspirations; USV syllables produced by prolonged-RAm^{VOC}-activation were periodically interrupted by full inspiration peaks (Fig. 4). We found that the inspiration rhythm generator preBötC, where *Vgat+* and *GlyT2+* neurons are found (*36, 43*), provides the main source of inhibitory inputs to RAm^{VOC} (Fig. 5). Chronic disinhibition of RAm^{VOC} in RAm^{VOC}-GFE3 experiments reduced the amplitudes of inspiratory gating during vocalization, produced hoarse sound in inspiration phases as well as spontaneous USVs in the absence of social context (Fig. 5 and fig. S6). Taken together, our results support a conceptual model (Fig. 5C) in which the timing of phonation is controlled by the combined activity of preBötC and RAm^{VOC}, with inspiration playing a dominant role in setting the basic rhythm of vocalization, while RAm^{VOC} driving vocal cord closure and modulating syllable durations within the limit set by inspiration. This mechanism produces the periodic alternating patterns of vocalization and inspiration. In human speech, multiple syllables can be uttered within one breath, and in that case, a separate multi-syllable rhythm generator within expiration period might be needed. We also labeled laryngeal premotor neurons in NTS (Fig. 1C), which is a region receiving inputs from vagal pulmonary afferents (*43*). It is possible that the pulmonary-NTS pathway is involved in the transition between inspiration and vocalization (*44*). When the lungs are inflated with enough air, this pathway may help to inhibit the activity of preBötC and facilitate the transition to vocalization and expiration. Future work should test whether the pulmonary-NTS circuit represents the third node in modulating vocal patterns.

Finally, we want to point out that our study focused only on the "phonation", but not the complex "articulation" aspect of vocalization. Vocal articulations are among the most complicated motor patterns generated by humans (and many mammals) as they require coordinated control of the laryngeal, facial, tongue, jaw, and respiratory muscles. How this is achieved remains poorly understood. In our transsynaptic tracing studies, we labeled a large population of neurons in the reticular formation, and we found that laryngeal premotor neurons also project to other orofacial motor nuclei (fig. S1). However, the identities of these premotor neurons are unknown, and more work will be needed to determine whether and how these neurons are involved in complex articulations.

References and Notes:

1. G. Holstege, H. H. Subramanian, Two different motor systems are needed to generate human speech. *Journal of Comparative Neurology* **524**, 1558-1577 (2016).
2. A. Nieder, R. Mooney, The neurobiology of innate, volitional and learned vocalizations in mammals and birds. *Philosophical Transactions of the Royal Society B: Biological Sciences* **375**, 20190054 (2020).
3. Z. Zhang, Mechanics of human voice production and control. *The Journal of the Acoustical Society of America* **140**, 2614-2635 (2016).
4. C. A. Del Negro, G. D. Funk, J. L. Feldman, Breathing matters. *Nature Reviews Neuroscience* **19**, 351-367 (2018).
5. K. L. Christopher *et al.*, Vocal-Cord Dysfunction Presenting as Asthma. *New England Journal of Medicine* **308**, 1566-1570 (1983).
6. J. M. Hintze, C. L. Ludlow, S. F. Bansberg, C. H. Adler, D. G. Lott, Spasmodic Dysphonia: A Review. Part 2: Characterization of Pathophysiology. *Otolaryngology–Head and Neck Surgery* **157**, 558-564 (2017).
7. U. Jürgens, S. R. Hage, On the role of the reticular formation in vocal pattern generation. *Behavioural Brain Research* **182**, 308-314 (2007).
8. K. Shiba, T. Umezaki, Y. Zheng, A. D. Miller, The nucleus retroambigualis controls laryngeal muscle activity during vocalization in the cat. *Experimental Brain Research* **115**, 513-519 (1997).
9. S. P. Zhang, R. Bandler, P. J. Davis, Brain stem integration of vocalization: role of the nucleus retroambigualis. *Journal of Neurophysiology* **74**, 2500-2512 (1995).
10. K. Hartmann, M. Brecht, A Functionally and Anatomically Bipartite Vocal Pattern Generator in the Rat Brain Stem. *iScience* **23**, (2020).
11. S. P. Zhang, P. J. Davis, P. Carrive, R. Bandler, Vocalization and marked pressor effect evoked from the region of the nucleus retroambigualis in the caudal ventrolateral medulla of the cat. *Neuroscience Letters* **140**, 103-107 (1992).
12. L. Lüthe, U. Häusler, U. Jürgens, Neuronal activity in the medulla oblongata during vocalization. A single-unit recording study in the squirrel monkey. *Behavioural Brain Research* **116**, 197-210 (2000).
13. M. Concha-Miranda, W. Tang, K. Hartmann, M. Brecht, Large-Scale Mapping of Vocalization-Related Activity in the Functionally Diverse Nuclei in Rat Posterior Brainstem. *The Journal of Neuroscience* **42**, 8252-8261 (2022).
14. G. Holstege, Anatomical study of the final common pathway for vocalization in the cat. *Journal of Comparative Neurology* **284**, 242-252 (1989).
15. H. H. Subramanian, G. Holstege, The Nucleus Retroambiguus Control of Respiration. *The Journal of Neuroscience* **29**, 3824-3832 (2009).
16. Y. Cui *et al.*, Defining preBötzinger Complex Rhythm- and Pattern-Generating Neural Microcircuits In Vivo. *Neuron* **91**, 602-614 (2016).
17. A. Huff, M. Karlen-Amarante, T. Pitts, J. M. Ramirez, Optogenetic stimulation of pre–Bötzinger complex reveals novel circuit interactions in swallowing–breathing coordination. *Proceedings of the National Academy of Sciences* **119**, e2121095119 (2022).
18. D. Sherman, J. W. Worrell, Y. Cui, J. L. Feldman, Optogenetic perturbation of preBötzinger complex inhibitory neurons modulates respiratory pattern. *Nature Neuroscience* **18**, 408-414 (2015).

19. J. C. Smith, H. H. Ellenberger, K. Ballanyi, D. W. Richter, J. L. Feldman, Pre-Bötzinger Complex: a Brainstem Region that May Generate Respiratory Rhythm in Mammals. *Science* **254**, 726-729 (1991).
20. S. Tupal *et al.*, Testing the role of preBötzinger Complex somatostatin neurons in respiratory and vocal behaviors. *European Journal of Neuroscience* **40**, 3067-3077 (2014).
21. G. Arriaga, E. D. Jarvis, Mouse vocal communication system: Are ultrasounds learned or innate? *Brain and Language* **124**, 96-116 (2013).
22. T. E. Holy, Z. Guo, Ultrasonic Songs of Male Mice. *PLOS Biology* **3**, e386 (2005).
23. M. Fernández-Vargas, T. Riede, B. Pasch, Mechanisms and constraints underlying acoustic variation in rodents. *Animal Behaviour* **184**, 135-147 (2022).
24. J. Håkansson *et al.*, Aerodynamics and motor control of ultrasonic vocalizations for social communication in mice and rats. *BMC Biology* **20**, 3 (2022).
25. E. Mahrt, A. Agarwal, D. Perkel, C. Portfors, C. P. H. Elemans, Mice produce ultrasonic vocalizations by intra-laryngeal planar impinging jets. *Current Biology* **26**, R880-R881 (2016).
26. T. Riede, H. L. Borgard, B. Pasch, Laryngeal airway reconstruction indicates that rodent ultrasonic vocalizations are produced by an edge-tone mechanism. *Royal Society Open Science* **4**, 170976 (2017).
27. J. Takatoh *et al.*, Constructing an adult orofacial premotor atlas in Allen mouse CCF. *eLife* **10**, e67291 (2021).
28. Q. Wang *et al.*, The Allen Mouse Brain Common Coordinate Framework: A 3D Reference Atlas. *Cell* **181**, 936-953.e920 (2020).
29. K. Sakurai *et al.*, Capturing and Manipulating Activated Neuronal Ensembles with CANE Delineates a Hypothalamic Social-Fear Circuit. *Neuron* **92**, 739-753 (2016).
30. G. G. Schiavo *et al.*, Tetanus and botulinum-B neurotoxins block neurotransmitter release by proteolytic cleavage of synaptobrevin. *Nature* **359**, 832-835 (1992).
31. J. Ruat *et al.*, Why do mice squeak? Toward a better understanding of defensive vocalization. *iScience* **25**, 104657 (2022).
32. K. Tschida *et al.*, A Specialized Neural Circuit Gates Social Vocalizations in the Mouse. *Neuron* **103**, 459-472.e454 (2019).
33. C. Hérent, S. Diem, G. Fortin, J. Bouvier, Absent phasing of respiratory and locomotor rhythms in running mice. *eLife* **9**, e61919 (2020).
34. K. E. Kishi *et al.*, Structural basis for channel conduction in the pump-like channelrhodopsin ChRmine. *Cell* **185**, 672-689.e623 (2022).
35. A. H. O. Fonseca, G. M. Santana, G. M. Bosque Ortiz, S. Bampi, M. O. Dietrich, Analysis of ultrasonic vocalizations from mice using computer vision and machine learning. *eLife* **10**, e59161 (2021).
36. C. F. Yang, J. L. Feldman, Efferent projections of excitatory and inhibitory preBötzinger Complex neurons. *Journal of Comparative Neurology* **526**, 1389-1402 (2018).
37. G. G. Gross *et al.*, An E3-ligase-based method for ablating inhibitory synapses. *Nature Methods* **13**, 673-678 (2016).
38. I. A. Volodin, D. D. Yurlova, O. G. Ilchenko, E. V. Volodina, Ontogeny of audible squeaks in yellow steppe lemming Eolagurus luteus: trend towards shorter and low-frequency calls is reminiscent of those in ultrasonic vocalization. *BMC Zoology* **6**, 27 (2021).

39. M. Smotherman, K. Kobayasi, J. Ma, S. Zhang, W. Metzner, A Mechanism for Vocal-Respiratory Coupling in the Mammalian Parabrachial Nucleus. *The Journal of Neuroscience* **26**, 4860-4869 (2006).
40. J. W. Arthurs, A. J. Bowen, R. D. Palmiter, N. A. Baertsch, Parabrachial tachykinin1-expressing neurons involved in state-dependent breathing control. *Nature Communications* **14**, 963 (2023).
41. S. Liu *et al.*, Divergent brainstem opioidergic pathways that coordinate breathing with pain and emotions. *Neuron* **110**, 857-873.e859 (2022).
42. X. P. Wei, M. Collie, B. Dempsey, G. Fortin, K. Yackle, A novel reticular node in the brainstem synchronizes neonatal mouse crying with breathing. *Neuron* **110**, 644-657.e646 (2022).
43. K. Yackle, Transformation of Our Understanding of Breathing Control by Molecular Tools. *Annual Review of Physiology* **85**, 93-113 (2023).
44. K. Nakazawa *et al.*, Role of pulmonary afferent inputs in vocal on-switch in the cat. *Neuroscience Research* **29**, 49-54 (1997).
45. F. Claudi et al., bioRxiv, 2020.2002.2023.961748 (2020).
46. J. Takatoh et al., Nature 609, 560 (2022).
47. T. Nath et al., Nature Prot. 14, 2152 (2019).

Acknowledgments: We thank David Kleinfeld, Vincent Prevosto, Paul Thompson for critically reading the manuscript. We thank the Wang lab members for many technical help and suggestions during the entire process of this research project. We thank Richard Mooney lab for stimulating discussion on vocalization circuits and mechanisms.

Funding:

National Institutes of Health grants MH117778 (to F.W) and NS107466 (a team grant with a subaward to F.W)

Author contributions:

F.W. and J.P conceptualized the project, designed experiments, and wrote the paper with input from all authors. J.P. performed the majority of experiments. J.P. and J.T. analyzed data. S.C. performed histology works. S.Z., A.H., and J.T. produced key viral vectors used in this study. B.H. and S.C. provided animal husbandry. F.W. supervised all the work.

Competing interests:

The authors declare no competing interests.

Data and materials availability:

All data and code are available in the main text, the supplementary materials, or Dryad (https://doi.org/10.5061/dryad.vmcvdnd0m).

Supplementary Materials

Materials and Methods

Figs. S1 to S6

Movies S1 to S3

References (46-48)

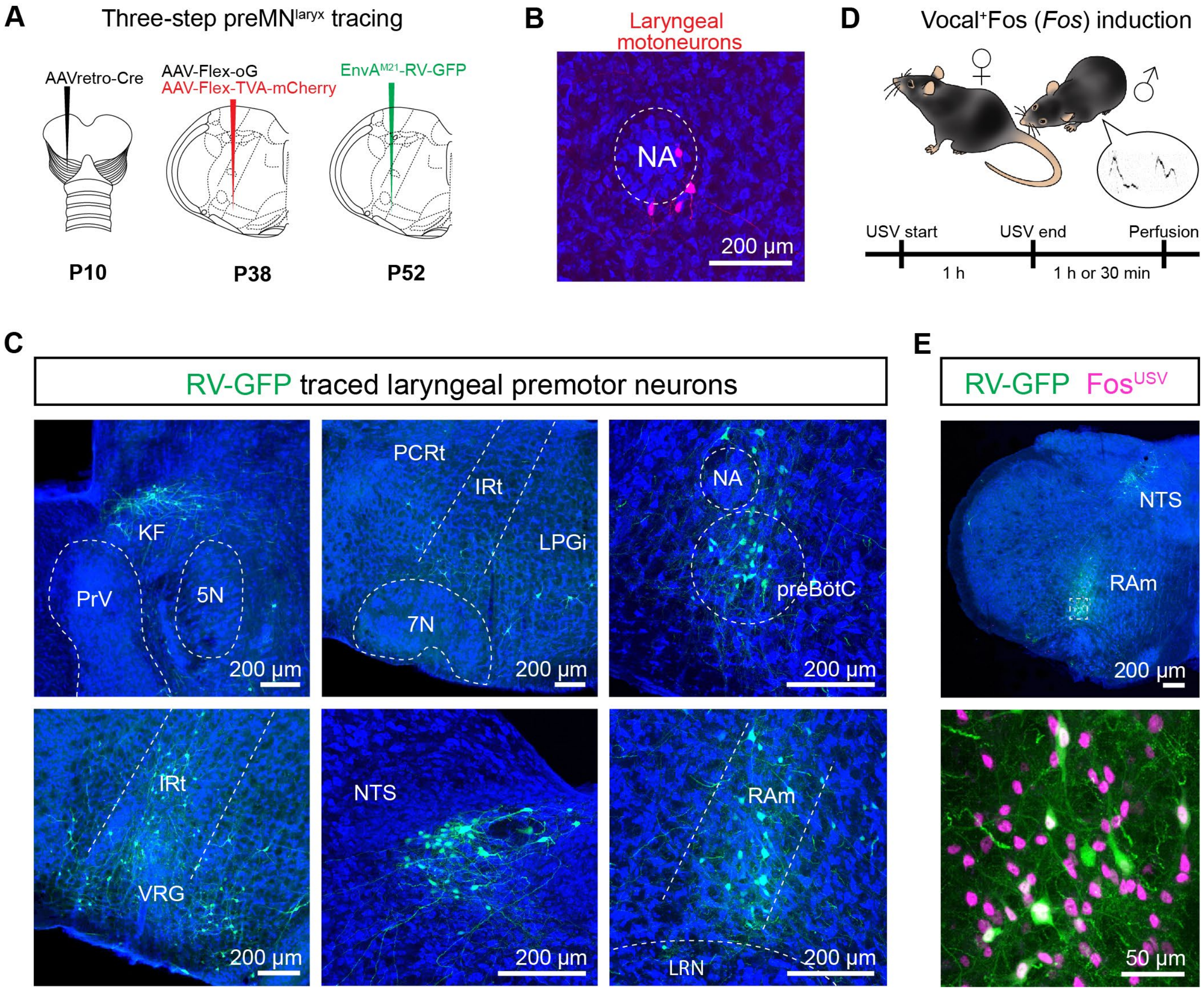
A
Three-step preMN^{laryx} tracing
AAVretro-Cre
AAV-Flex-oG
AAV-Flex-TVA-mCherry
EnvA^{M21}-RV-GFP
P10
P38
P52
B
Laryngeal motoneurons
NA
200 µm
D
Vocal^{+}Fos (*Fos*) induction
♀
♂
USV start
USV end
Perfusion
1 h
1 h or 30 min
C
RV-GFP traced laryngeal premotor neurons
KF
PrV
5N
200 µm
PCRt
IRt
LPGi
7N
200 µm
NA
preBötC
200 µm
IRt
VRG
200 µm
NTS
200 µm
RAm
LRN
200 µm
E
RV-GFP Fos^{USV}
NTS
RAm
200 µm
50 µm

Fig. 1. Transsynaptic mapping of laryngeal premotor neurons and vocalization-induced Fos activity in the RAm.

(A) A schematic for three-step monosynaptic rabies virus strategy using AAVretro-Cre, helper virus (AAV-Flex-oG, AAV-Flex-TVA-mCherry), and monosynaptic rabies virus (EnvA^{M21} coated) to map laryngeal premotor neurons. (B) Laryngeal motoneurons (red) labeled by AAVretro-Cre in the brainstem of an Ai-14 reporter mouse. (C) Laryngeal premotor neurons (green) in the KF, PCRt, LPGi, preBötC, IRt, VRG, NTS, and RAm. (D) A schematic for Fos (for 1h) or *Fos* mRNA (30min) induction experiments in a social-context eliciting USVs in male mice. (E) Laryngeal premotor neurons (green) and Fos (magenta) labeling in the RAm (upper). A zoomed-image of the boxed area (bottom). Neurotrace Blue was used to visualize neuronal structures. Scale bars, 200 µm (B, C, E upper); 50 µm (E bottom).

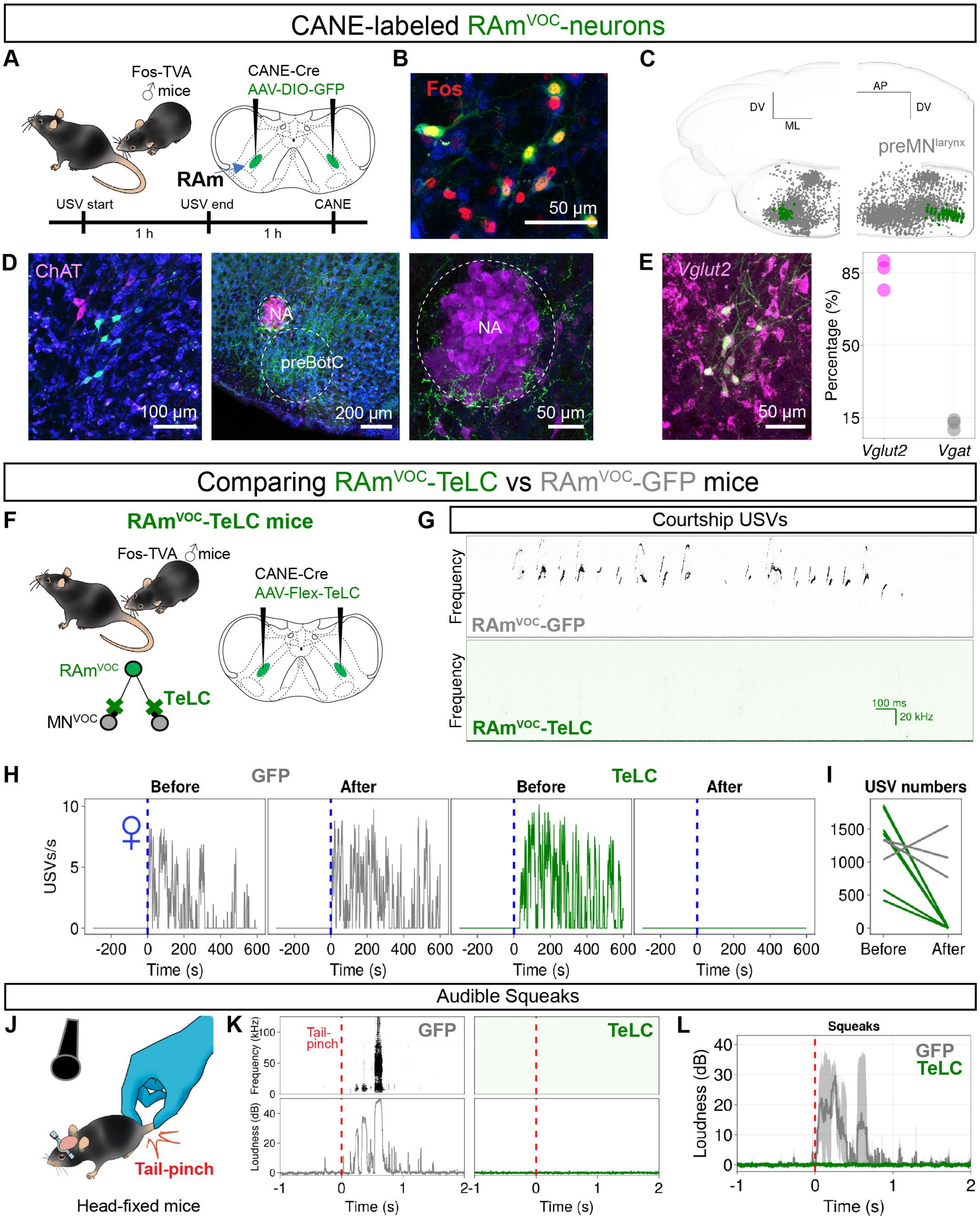
CANE-labeled RAmVOC-neurons
A
Fos-TVA
♂ mice
CANE-Cre
AAV-DIO-GFP
RAm
USV start
USV end
CANE
1 h
1 h
B
Fos
50 µm
C
DV
ML
AP
DV
preMNlarynx
D
ChAT
100 µm
NA
preBotC
200 µm
NA
50 µm
E
Vglut2
50 µm
85
50
15
Percentage (%)
Vglut2
Vgat
Comparing RAmVOC-TeLC vs RAmVOC-GFP mice
F
RAmVOC-TeLC mice
Fos-TVA ♂mice
CANE-Cre
AAV-Flex-TeLC
RAmVOC
TeLC
MNVOC
G
Courtship USVs
Frequency
RAmVOC-GFP
Frequency
RAmVOC-TeLC
100 ms
20 kHz
H
GFP
Before
After
TeLC
Before
After
♀
USVs/s
10
5
0
-200
0
200
400
600
Time (s)
I
USV numbers
1500
1000
500
0
Before
After
Audible Squeaks
J
Tail-pinch
Head-fixed mice
K
Tail-pinch
GFP
TeLC
Frequency (kHz)
100
50
0
Loudness (dB)
40
20
0
-1
0
1
2
Time (s)
L
Squeaks
GFP
TeLC
Loudness (dB)
40
30
20
10
0
-1
0
1
2
Time (s)

Fig. 2. Vocalization-induced Fos positive neurons in the RAm (RAm^{VOC}-neurons) are excitatory laryngeal premotor neurons and required for vocalization in mice.

(A) A schematic for CANE experiments to capture vocalization-induced Fos positive neurons in the RAm. (B) RAm^{VOC}-neurons (green) with Fos immunolabeling (red). (C) RAm^{VOC}-neurons (green) with the laryngeal premotor neurons (grey) in the Allen CCF in coronal (left) and sagittal (right) views. (D) RAm^{VOC}-neurons (green) with ChAT immunolabeling (magenta). Left (soma) and middle (axon terminals). The right panel highlights the NA region of the middle panel. (E) RAm^{VOC}-neurons (green) with fluorescent in situ hybridization labeling for *Vglut2* (magenta) (left). Group data of *Vglut2* and *Vgat* from n=3 mice. (F) A schematic for expressing TeLC in RAm^{VOC}-neurons. (G) Spectrograms of female-directed USVs of RAm^{VOC}-GFP controls (upper) and RAm^{VOC}-TeLC (bottom) mice. (H) USV rates of male mice during courtship behaviors for 10 min. Blue vertical lines indicate the time of female introduction (♀). Grey and green plots for a RAmVOC-GFP mouse and a RAm^{VOC}-TeLC mouse, before and 2 weeks after virus injection (left and right, respectively). (I) The total numbers of USV syllables during 10min social interactions (RAm^{VOC}-TeLC, green, n=6; and control, grey, n=3). (J) A schematic for recording tail pinch-induced audible squeaks. (K) Spectrogram (upper) and sound intensity plots (bottom) of audible squeaks from RAm^{VOC}-GFP (grey, left) and RAm^{VOC}-TeLC (green, right) mice. Red vertical lines indicate the onset of tail-pinch stimuli. (L) Average intensity of squeaks during tail-pinch (n=3 for each group).

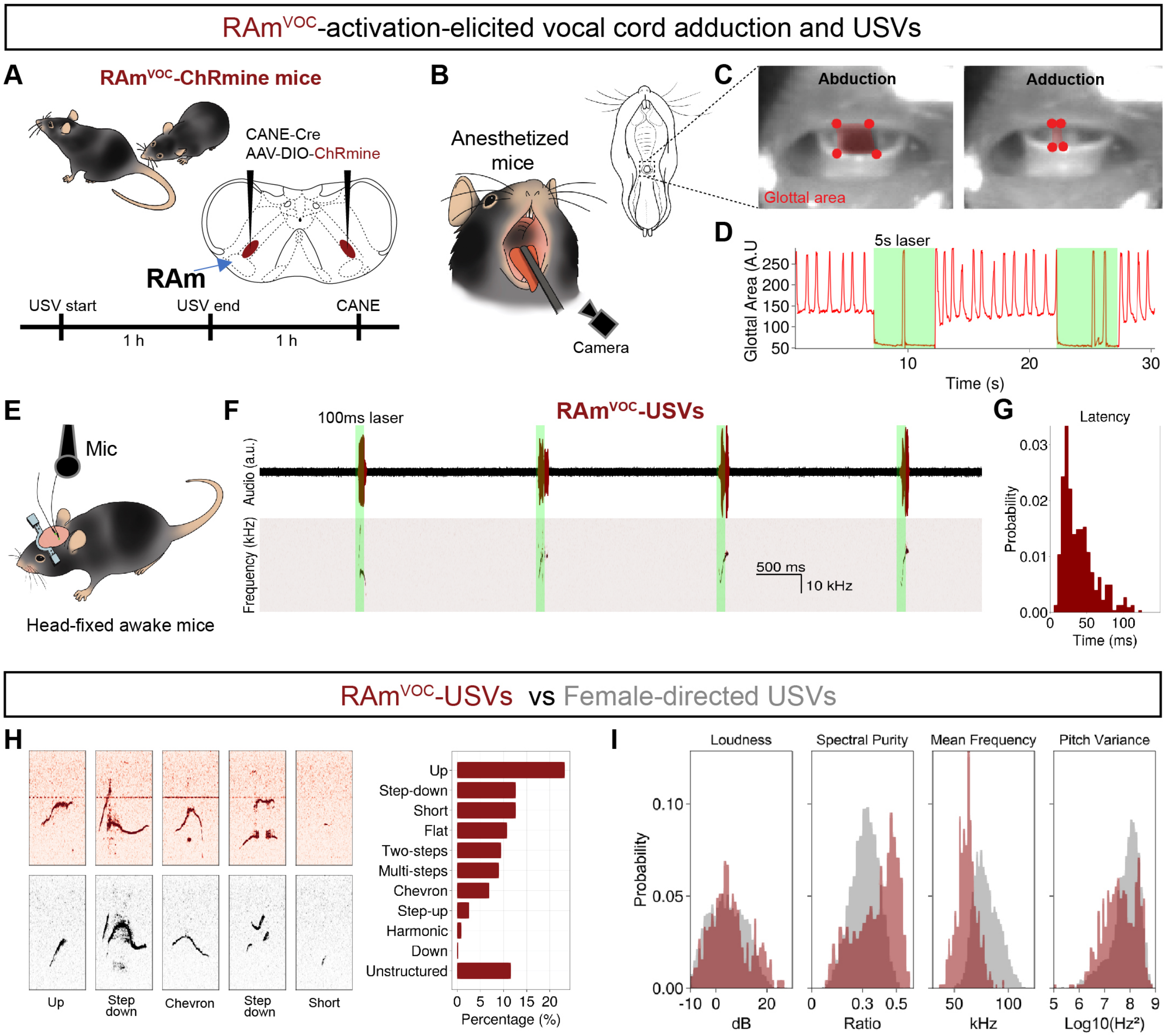
RAm^{VOC}-activation-elicited vocal cord adduction and USVs
A
RAm^{voc}-ChRmine mice
CANE-Cre
AAV-DIO-ChRmine
RAm
USV start
USV end
CANE
1 h
1 h
B
Anesthetized mice
Camera
C
Abduction
Adduction
Glottal area
D
5s laser
Glottal Area (A.U
250
200
150
100
50
10
20
30
Time (s)
E
Mic
Head-fixed awake mice
F
100ms laser
RAm^{voc}-USVs
Audio (a.u.)
Frequency (kHz)
500 ms
10 kHz
G
Latency
Probability
0.03
0.02
0.01
0.00
0
50
100
Time (ms)
RAm^{VOC}-USVs vs Female-directed USVs
H
Up
Step down
Chevron
Step down
Short
Up
Step-down
Short
Flat
Two-steps
Multi-steps
Chevron
Step-up
Harmonic
Down
Unstructured
0
5
10
15
20
Percentage (%)
I
Loudness
Spectral Purity
Mean Frequency
Pitch Variance
Probability
0.10
0.05
0.00
-10
0
20
dB
0
0.3
0.5
Ratio
50
100
kHz
5
6
7
8
9
Log10(Hz²)

Fig. 3 Optogenetic activation of RAm^{VOC}-neurons robustly elicits USV-like vocalizations in mice.

(A) Schematic for expressing ChRmine to RAm^{VOC}-neurons using CANE method. (B) Schematic for visualizing the vocal cords in anesthetized mice. (C) Images showing opened (left) and closed (right) vocal cords. Red dots indicate the cartilage parts of the vocal cords that are used to track the glottal area (red rectangle). (D) The response of the glottal area to RAm^{VOC}-opto-activation. Green bar (5s) indicates the laser stimulation period. E) Schematic for recording vocalization of awake mice in a head-fixed condition. F) Sound-time raw traces (upper) and corresponding frequency-time spectrogram (bottom) during a train of brief laser pulses (laser wavelength = 560nm, 100ms of 4 pulses with 2s intervals). (G) Latency distribution of RAm^{VOC}-USVs (laser duration:100ms, 443 syllables, n=3 mice). (H) Examples of RAm^{VOC} (left upper row, red) and female-directed USVs (left bottom row, grey). A single box spans 120ms (x axis) and 30 to 125kHz (y axis). Classification results of RAm^{VOC}-USVs (right). (I) Distributions of four acoustic features (loudness, spectral purity, mean frequency, and pitch variance) of RAm^{VOC}-USVs (443 syllables, n=3 mice) and female-directed USVs (4960 syllables, n=3 mice).

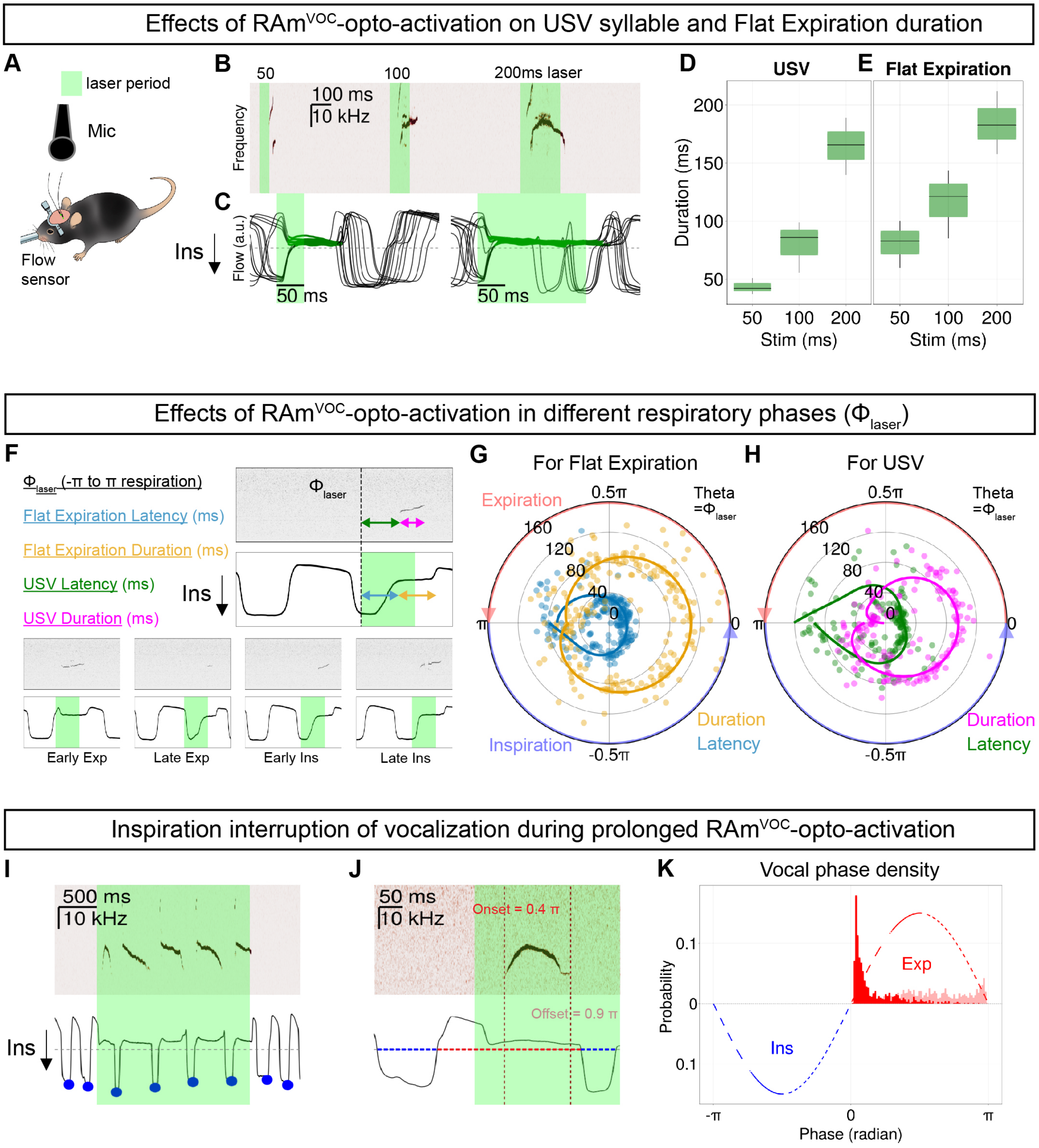
Effects of RAm^VOC-opto-activation on USV syllable and Flat Expiration duration
A
laser period
Mic
Flow sensor
B
50
100
200ms laser
100 ms
10 kHz
Frequency
C
Ins
Flow (a.u.)
50 ms
50 ms
D
USV
E
Flat Expiration
Duration (ms)
200
150
100
50
50 100 200
Stim (ms)
50 100 200
Stim (ms)
Effects of RAm^VOC-opto-activation in different respiratory phases (Φ_laser)
F
Φ_laser (-π to π respiration)
Flat Expiration Latency (ms)
Flat Expiration Duration (ms)
USV Latency (ms)
USV Duration (ms)
Φ_laser
Ins
Early Exp
Late Exp
Early Ins
Late Ins
G
For Flat Expiration
Expiration
0.5π
Theta =Φ_laser
160
120
80
40
0
π
0
Inspiration
-0.5π
Duration
Latency
H
For USV
0.5π
Theta =Φ_laser
160
120
80
40
0
π
0
-0.5π
Duration
Latency
Inspiration interruption of vocalization during prolonged RAm^VOC-opto-activation
I
500 ms
10 kHz
Ins
J
50 ms
10 kHz
Onset = 0.4 π
Offset = 0.9 π
K
Vocal phase density
Probability
0.1
0
0.1
Exp
Ins
-π
0
π
Phase (radian)

Fig. 4 RAm^{VOC}-activation can modulate the duration of USVs and concurrent expiratory periods until interrupted by the need for breathing.

(A) Schematic for recording vocalization and respiration in RAm^{VOC}-ChRmine mice. (B) USV syllables evoked by three different durations of RAm^{VOC} laser activation (50, 100, and 200ms). (C) Respiratory responses to the RAm^{VOC}-activation (Left: 50ms, Right: 200ms). 13 trials are aligned to the laser onsets and overlayed. Green lines indicate RAm^{VOC}-induced flat expiration periods. (D) Average duration of RAm^{VOC}-USVs (n=3 mice). (E) Average duration of RAm^{VOC}-induced flat expiration periods (n=3 mice). (F) A schematic for defining laser stimulation phase (Φ_{laser}) and latency and duration of RAm^{VOC}-induced flat expiration and USV to stimulation (upper). Black trace indicates normalized airflow. Φ_{laser} is defined as a phase of laser onsets with respect to the expected airflow (Inspiration: -π to 0, Expiration: 0 to π). Four cases of different stimulation onset phases (bottom). (G) Relationship between Φ_{laser}, and latency and duration of RAm^{VOC}-expirations (rho, ms scale). The same-color solid lines represent polynomial-fitted lines. Red and blue circle-arrows indicate the expiration (0 to π) and inspiration phases (-π to 0), respectively. (H) Relationship between Φ_{laser}, and latency and duration of RAm^{VOC}-USVs. (I) USVs (upper) and respiratory responses (bottom) to the 2s RAm^{VOC}-activation. Blue dots indicate the inspiratory flow peaks. (J) Projection of onset and offset of a RAm^{VOC}-USV onto a respiratory phase. (k) Phase density distribution of the onsets (red) and offsets (pink) of RAm^{VOC}-USVs. Blue and red dash lines represent arbitrary inspiration and expiration phase, respectively.

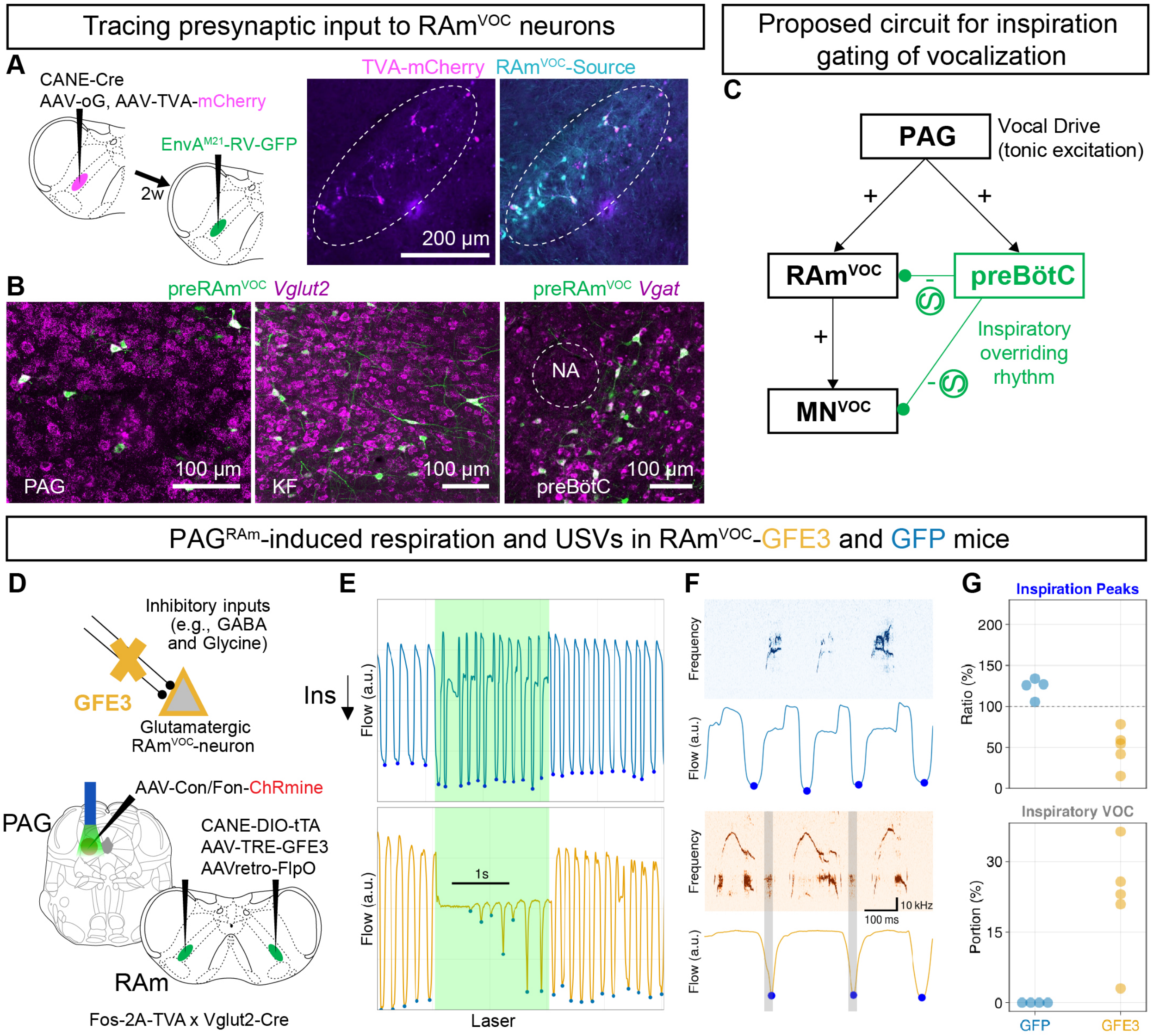
Tracing presynaptic input to RAmVOC neurons
A
CANE-Cre
AAV-oG, AAV-TVA-mCherry
EnvAM21-RV-GFP
2w
TVA-mCherry
RAmVOC-Source
200 µm
B
preRAmVOC Vglut2
preRAmVOC Vgat
PAG
100 µm
KF
100 µm
NA
preBötC
100 µm
Proposed circuit for inspiration gating of vocalization
C
PAG
Vocal Drive
(tonic excitation)
+
+
RAmVOC
preBötC
-
+
Inspiratory overriding rhythm
-
MNVOC
PAGRAm-induced respiration and USVs in RAmVOC-GFE3 and GFP mice
D
Inhibitory inputs
(e.g., GABA and Glycine)
GFE3
Glutamatergic RAmVOC-neuron
AAV-Con/Fon-ChRmine
PAG
CANE-DIO-tTA
AAV-TRE-GFE3
AAVretro-FlpO
RAm
Fos-2A-TVA x Vglut2-Cre
E
Ins
Flow (a.u.)
Flow (a.u.)
1s
Laser
F
Frequency
Flow (a.u.)
Frequency
10 kHz
100 ms
Flow (a.u.)
G
Inspiration Peaks
Ratio (%)
200
150
100
50
0
Inspiratory VOC
Portion (%)
30
15
0
GFP
GFE3

Fig. 5 Ablating inhibitory synapses on RAm$^{\mathrm{VOC}}$-neurons compromised vocal-respiratory coordination.

(A) Schematic for transsynaptically tracing preRAm$^{\mathrm{VOC}}$-neurons (left). CANE and rabies labeled-source cells (magenta: TVA, cyan: GFP) in RAm (right). Dash-circles indicate RAm areas. (B) preRAm$^{\mathrm{VOC}}$-neurons (green) in the PAG, KF, and preBötC with in situ hybridization (magenta for *Vglut2* and *Vgat*). (C) Schematic for the proposed neural mechanism for vocal-respiratory coordination. (D) Schematic for ablating inhibitory synapses in RAm$^{\mathrm{VOC}}$-neurons with GFE3 expression (RAm$^{\mathrm{VOC}}$-GFE3), and concurrent expression of ChRmine in RAm projecting glutamatergic PAG neurons. (E) Respiratory activities of the RAm$^{\mathrm{VOC}}$-GFP (blue) and RAm$^{\mathrm{VOC}}$-GFE3 (orange) mice in response to the PAG$^{\mathrm{RAm/vglut2}}$-ChRmine stimulation for 2s. Blue dots represent the inspiratory peaks. (F) Spectrogram (upper) with the respiratory responses (bottom). Grey bars label abnormal vocalizations in the inspiratory phases. (G) Average changes in the inspiratory peaks of the mice (n=5, GFE3; n=4, GFP, upper) during the PAG$^{\mathrm{RAm/vglut2}}$ stimulation over the baseline inspirations. The portions of the abnormal inspiratory vocalization among the PAG$^{\mathrm{RAm/vglut2}}$-induced vocalizations (n=5, GFE3; n=4, GFP, bottom). No inspiratory vocalization was detected in the GFP control mice.

Science
AAAS

Supplementary Materials for

Brainstem control of vocalization and its coordination with respiration

Jaehong Park[1,2*], Seonmi Choi[1], Jun Takatoh[1], Shengli Zhao[3], Andrew Harrahill[1], Bao-Xia Han[3], Fan Wang[1*]

Corresponding authors: Fan Wang (fan_wang@mit.edu) or Jaehong Park (jaehong@mit.edu)

The PDF file includes:

Materials and Methods
Figs. S1 to S6
References (46-48)

Other Supplementary Materials for this manuscript include the following:

MDAR Reproducibility Checklist
Movies S1 to S3

Materials and Methods

Experimental models and subject details

All animal experiments were performed in accordance with the MIT Committee for Animal Care Use Committee and Duke University Institutional Animal Care. Pups (postnatal 10 ~17 days) of either C57BL/6 or tdTomato reporter mice (Ai14, Stock No: 007914, Jackson laboratory) were used for tracing premotor neurons of the laryngeal muscles. Male homozygous $\mathrm{Fos}^{\mathrm{TVA}}$ (Stock No: 027831, Jackson laboratory) were used for most of CANE experiments except for $\mathrm{preRAm}^{\mathrm{VOC}}$ tracing. Male heterozygous $\mathrm{Fos}^{\mathrm{TVA}}$ (crossed with C57BL/6 background) were used for $\mathrm{preRAm}^{\mathrm{VOC}}$ tracing. Vglut2-ires-Cre mice (Stock No: 016963, Jackson laboratory) were crossed with $\mathrm{Fos}^{\mathrm{TVA}}$ mice to obtain $\mathrm{Fos}^{\mathrm{TVA}}$ (het)/Vglut2-ires-Cre (het) for a subset of experiments.

Viruses

AAV2retro-pENN.AAV.hSyn.Cre.WPRE.hGH (Addgene #105553)
AAV2retro-phSyn1(S)-FlpO-bGHpA (Addgene #51669)
AAV2/8-CAG-Flex-oG (Addgene #48332, Duke Viral Vector Core)
AAV2/8-CAG-Flex-TVA-mCherry (Addgene #74292, Duke Viral Vector Core)
AAV2/8-hSyn-Flex-TeLC-P2A-EYFP-WPRE (Addgene #135391)
AAV2/8-hSyn-DIO-EGFP (Addgene #50457)
AAV2/8-nEF-Con/Foff 2.0-ChRmine-oScarlet (Addgene #137161)
AAV2/8-nEF-Con/Fon-ChRmine-oScarlet (Addgene # 137159)
AAV2/8-nEF-Coff/Fon-ChRmine-oScarlet (Addgene # 137160)
AAV2/8-TRE3G-GFP-GFE3 (This study)
AAV2/8-TRE3G-EGFP (This study)
EnvA (M21)-RV-ΔG-GFP (30)
CANE (lenti)-hSyn-Cre (30)
CANE (lenti)-hSyn-DIO-tTA (This study)

Method details

Stereotaxic virus injection surgery

Mice were initially anesthetized by isoflurane (3%), then further maintained by isoflurane (1-2%) until the surgeries ended. The heads of mice were fixed at a stereotaxic frame (Model 963, David Kopf Instruments), and the body temperatures were maintained at 37°C with a heating pad. The virus solution was stereotaxically injected with a pulled-glass pipette (Drummond, 5-000-2005) using an oil-hydraulic pump (MO-10, Narishige).

Stereotaxic coordinates

Anterior-Posterior and Medial-Lateral coordinates are from the Bregma. Dorsal-Ventral coordinates are from the brain surface.

Nucleus ambiguous (NA): AP: -6.4 mm, ML: -1.2 mm, DV: -4.8 mm
RAm: AP: -5.8 mm, ML: 1.2 mm, DV: -5.4 mm (20° AP angle)
PAG: AP: -3.3 mm, ML: 0.6 mm, DV: -2.4 mm (30° AP angle)

Head-post and optic fiber implantation

In cases of the head-fixed or optogenetic experiments, mice were implanted with a head post (custom made steel). For optogenetic manipulations, optic cannulas (200 µm core, 0.4NA, RWD

Life Science) were implanted. The implantations were performed right after the virus injections. Dental cement (C&B Metabond) was applied to the skulls to secure the implantations.

Three-step monosynaptic tracing for premotor neurons of laryngeal muscles in adult mice

Laryngeal premotor neurons in adult mice were traced by the three-step monosynaptic rabies virus tracing as previously described (23). Briefly, mice pups were anesthetized by isoflurane (3% for induction and 1.5% for maintenance). Midline incision in the neck skin and sternohyoid muscle was performed, and the incised sternohyoid muscle was bilaterally retracted with thin thread to expose the larynx. AAV2retro-hSyn-Cre was injected into laryngeal muscles (500 nl) using a quartz micropipette (Sutter Instrument) through a micro syringe pump system (UMP3 and Micro4; WPI). Three weeks or more after the AAV injection, a mixture of AAV2/8-CAG-Flex-oG and AAV2/8-CAG-Flex-TVA-mCherry (120nl total with 1:1 ratio in volume) was stereotaxically injected in the ipsilateral NA. Two weeks later, EnvA (M21)-RV-ΔG-GFP (200 nl) was injected in the same injection target. After 5 days, the mice were perfused for histology.

Registering neurons in the Allen CCF

Registrations of laryngeal premotor and RAm^{VOC} neurons were performed as described previously (23). Briefly, all neurons in serial-sectioned (80 µm) brain slices were manually registered to generate 3D coordinates in the Allen CCF with custom-written MATLAB. A Python package, Brainrender2 (*45*) was used to visualize neurons in 3D.

Analysis of spatial distribution and correlation

As previously described (23), a kernel density estimation in three-dimension was applied to the 3D-coordinates of registered cells. For 2D density plots, the 3D density estimations were projected to 2D dimension (AP, ML, or DV). The 3D density estimations were vectorized, then cosine similarities were calculated between each premotor map to plot a cross-correlogram. The coordinates of jaw and tongue premotor neurons were obtained from previous work.

Histology

Mice were anesthetized with an overdose of isoflurane and perfused with ice cold 1xPBS, followed by 4% PFA. The brains were frozen in OCT compound (Sakura Finetek). Eighty-micron serial coronal sections were made. Neurotrace blue (1:500, Thermo Fisher Scientific, N21479) was used to visualize neuronal structures.

Immunohistochemistry (IHC) for ChAT and Fos

Free-floating IHC was performed as previously described (*46*). Coronal brain slices were permeabilized for 3 hours in 1% Triton X in PBS (PBST), followed by the blocking solution (10% Blocking One (Nacalai Tesque) in 0.3% PBST). Floating sections were incubated at 4 degrees for 24 hours with the primary antibody in the blocking solution, then washed with 1xPBS three times for 10 mins each. Secondary antibodies in the blocking solution were applied to the sections for 24 hours at 4 degrees. Tissue sections were rinsed with 1xPBS three times for 10min each. The washed sections were mounted on slides with Mowiol. Antibodies for ChAT staining: primary (Goat, 1:500, AB144P, Sigma) and secondary (anti-Goat, 1:500, Alexa Fluor™ 555, A21432, Invitrogen). Antibodies for Fos staining: primary (Rabbit, 1:4000, 2250S, cell signaling) and secondary (anti-Rabbit, 1: 500, Alexa Fluor™ Plus 647, A32795, Invitrogen).

Fluorescent HCR (v.3.0, Molecular Instruments) RNA-FISH

HCR was performed as previously described (*46*). In brief, floating brain sections were perfused in 70% Ethanol/PBS overnight at 4 °C. The sections were washed with DEPC-PBS for three min each. The sections were then treated with 5% SDS/DEPC-PBS for 45 min at room temperature. After rinsing in 2× SSC, the sections were incubated in 2× SSC for 15 min. The sections were then incubated in probe hybridization buffer for 30 min at 37 °C for 30 min, followed by incubation with probes (*Fos, Vglut2, Vgat*, Molecular Instruments) overnight at 37 °C. After washing in HCR probe wash buffer (four times for 15 min at 37 °C), the sections were rinsed in 2× SSC (twice for 5 min) and incubated in HCR amplification buffer for 30 min at room temperature. The sections were then incubated for 48 hours at 25 °C with appropriate hairpins conjugated with Alexa Fluor (denatured and snap-cooled according to manufacturer's instructions) to visualize hybridization signals. The washed sections with 2× SSC (twice) were mounted on slides with Mowiol.

Courtship male mice behaviors

Male mice were placed in a glass cylindrical chamber and acclimated for 10min before being introduced to female partners. Female mice were placed in the chamber for up to 1 hour. The behaviors of the mice were recorded with a camera at 20 frames/s. Ninety-minutes or two hours after introduction of female and the vocalization onsets, the male mice were perfused for *Fos* HCR or Fos immunostaining, respectively.

CANE based targeting of RAm^{VOC}-neurons

Prior to CANE mediated capturing of RAm^{VOC}, each virgin male Fos^{TVA} mouse was first exposed to a female mouse overnight and then isolated in a single chamber for one week to facilitate male vocalization in the subsequent courtship contexts. Male mice were introduced with receptive females in a cylindrical chamber to elicit USVs for up to one hour. Two hours after the vocalization onsets, CANE (lenti)-hSyn-Cre and Cre dependent AAV2/8-gene X (600 nl total with 4:1 ratio in volume; gene X: hSyn-Flex-TeLC-P2A-EYFP-WPRE, hSyn-DIO-EGFP, nEF-Con/Foff 2.0-ChRmine-oScarlet) were stereotaxically injected to the RAm. For specifically targeting excitatory Ram^{VOC} neurons, Fos^{TVA}/Vglut2-ires-cre mice were used, and CANE (lenti)-hSyn-DIO-tTA and AAV2/8-TRE3G-geneX (600 nl total with 4:1 ratio in volume; gene X: GFP-GFE3, GFP), were injected to the RAm.

PreRAm^{VOC} tracing

The procedure is the same as the other experiment using CANE to express helper viruses AAV2/8-CAG-Flex-oG and AAV2/8-CAG-Flex-TVA-mCherry in RAm^{VOC}, followed by stereotaxic injection of EnvA (M21)-RV-ΔG-GFP (200 nl) to RAm two weeks later.

Recording and analysis of USVs

USVs were recorded with a recording system for ultrasonic-range audio signals (CM16/CMPA48AAF-5V, Avisoft-Bioacoustics). The audio signals were digitized at 250 kHz with an analog-digital converter (PCIe-6321, National Instruments). Spectrogram of audio signals were calculated by the Short Time Fourier Transform algorithm (512 Hanning window with 25% overlap). USVs were detected by manual selection from the spectrograms within 30-125 kHz. Classification of RAm^{VOC}-USVs were manually performed based on the criteria previously described (34). Four acoustic features were calculated for each USV syllable: 1) loudness (average band power between minimum and maximum frequency of each USV syllable as dB (relative to background noise in the recording)), 2) spectral purity (relative power of dominant frequency), 3) mean frequency (averaged dominant frequency at each time point), and 4) pitch variance (the variance of dominant frequencies). Putative inspiratory vocalizations were manually selected, based on the two criteria: 1) time-locked to inspiration periods and 2) broad spectral representation.

Respiratory activity recording and analysis

Respiratory Activity was measured as previously described (5). Briefly, awake mice were head-fixed, and an airflow sensor (AMW330V, Honeywell) was closely positioned to the nose of the mice. Voltage signals from the sensor were recorded at 250 kHz (PCIe-6321, National Instruments) and down-sampled to 1kHz for analysis. All breathing signals were normalized by their resting states: the breathing signals were subtracted by the reference value (at no-flow) and divided by the standard deviation of the resting breathing. For labeling flat-expirations, custom Julia codes were used to automatically detect flatten respiratory periods. Each negative and positive period of the breathing signals was interpolated and labeled as inspiration ($-\pi$ to 0) and expiration (0 to π) phases, respectively. Inspiration peaks were defined as the minimum values during each inspiration period. The inspiration peaks were interpolated to visualize the amplitude changes over time in average.

Correlation between duration of USVs and expirations

A linear regression model was used to fit a model of duration of USVs and flat-expirations. R^2 was calculated to assess the model.

Calculation of laser stimulation phases

Laser stimulation phases with respect to respiration (Φ_{laser}) were similarly calculated as previously described (18). Briefly, each negative and positive period of the breathing signals was interpolated and labeled as inspiration ($-\pi$ to 0) and expiration (0 to π) phases, respectively. Laser stimulation time relative to the onset of the inspiration was projected on the prior (control) respiratory period to define Φ_{laser} as from $-\pi$ to π. Each latency and duration of RAm^{VOC}-USVs and expiration data with respect to the laser stimulation phases was polynomial fitted using CurveFit.jl package to visualize the curves of the data.

Respiratory phase maps of USVs

The onset and offset time of USV syllables were projected onto the respiratory phase map. Vocalizations are classified as inspiratory or expiratory vocalization based on the phase values (negative as inspiratory and positive as expiratory)

Pain-induced audible squeak experiments

Either tail-pinch or electrical foot shock were applied to the mice. For tail-pinch experiments, awake mice were head-fixed and allowed to run on a running wheel. Mice tails were gently grabbed with a globed-hand and further pinched to elicit squeaks. Respiratory activities of the mice were measured with the airflow sensor. For electrical foot shock experiments, mice were placed in a foot-shock chamber, and brief electrical foot shock were delivered to the mice (<2s, 0.5mA). The behaviors of the mice in the chamber were recorded with a camera (with audible mic) at 20 frames/s. The squeaks from both stimuli were audible and also represented in the USV spectrum range.

Abdominal EMG recordings

Mice were initially anesthetized by isoflurane (3%), then further maintained by intraperitoneal injection of the ketamine and xylazine mixture (1 and 0.1 mg/kg, respectively). The skin above abdominal muscles were shaved and opened to expose abdominal muscles. Teflon coated silver wires (bare diameter: 76.2 µm, AM systems cat. 785500) were used to record EMG. The insulation was removed from the tips of silver wires (2mm) for recording. Recording wire was inserted into the abdominal muscle, while reference wire was inserted between the skin and fascia above the muscle. AC Amplifier (DAM80, World Precision Instruments) was used to record EMG, and the voltages were filtered (high pass: 100Hz, low pass: 10kHz) and collected with the same DAQ board (PCIe-6321, National Instruments). The sampling rate for EMG was 250kHz for simultaneous recording of USVs. The voltage recordings were down-sampled to 20kHz for analysis. The root-mean-square filter was applied to visualize the EMG responses. Averaged EMG responses during PAG stimulation (2s) were normalized by averaged resting EMG responses (1s) to calculated PAG-evoked EMG.

Vocal cord imaging and analysis

Mice were initially anesthetized by isoflurane (3%), then further maintained by intraperitoneal injection of the ketamine and xylazine mixture (1 and 0.1 mg/kg, respectively). The heads of mice were fixed with clamps, and the mice were put on a flat platform. A round post was placed under the neck to keep the axis of the oral cavity and trachea straight. The tongue was gently pulled out and moved down with a flat metal depressor (custom made) to help visualize the vocal cords. An optic fiber was attached to the tip of the depressor to illuminate the inside of the oral cavities with a red LED (635 nm, Doric). A camera (acA640-750um, Basler) with a lens (Basler Lens, C23-3520-2M-S f50mm) was used to image the vocal cords. Vocal cords were imaged at 100 frames/sec. The glottal areas of the vocal cords were calculated by tracking the videos using DeepLabCut (*47*).

Optogenetic stimulation of $\mathrm{RAm}^{\mathrm{VOC}}$ and $\mathrm{PAG}^{\mathrm{RAm/Vglut2}}$

Awake mice were head-fixed on a running wheel, and respiratory activities and sound productions were measured together. Bilateral ($\mathrm{RAm}^{\mathrm{VOC}}$-ChRmine) optogenetic stimulation was applied through optic fibers (0.39 NA, 200um core). 560 nm laser (less than 10mW at the tips) was used, and the stimulation parameters were modulated by TTL pulses with PulsePals. In experiments with $\mathrm{RAm}^{\mathrm{VOC}}$-GFE3 or control mice, optogenetic stimulation of the PAG was used to elicit USVs in a head-fixed setup. AAV2retro-hSyn-FlpO was injected into the RAm, and Cre/Flp-codependent AAV2/8-nEF-Con/Fon-ChRmine-mScarlet was injected into the PAG.

Statistics

All data are represented in mean±s.e.m. Statistical analyses were performed in Julia using HypothesisTests.jl package. Non-parametric test, Mann-Whitney was used to compare respiratory modulation in $\mathrm{RAm}^{\mathrm{VOC}}$-TeLC and $\mathrm{RAm}^{\mathrm{VOC}}$-GFP mice; mean frequency of $\mathrm{RAm}^{\mathrm{VOC}}$-USVs over female-directed USVs; and changes in inspiration peaks in $\mathrm{RAm}^{\mathrm{VOC}}$-GFE3 and $\mathrm{RAm}^{\mathrm{VOC}}$-GFP mice.

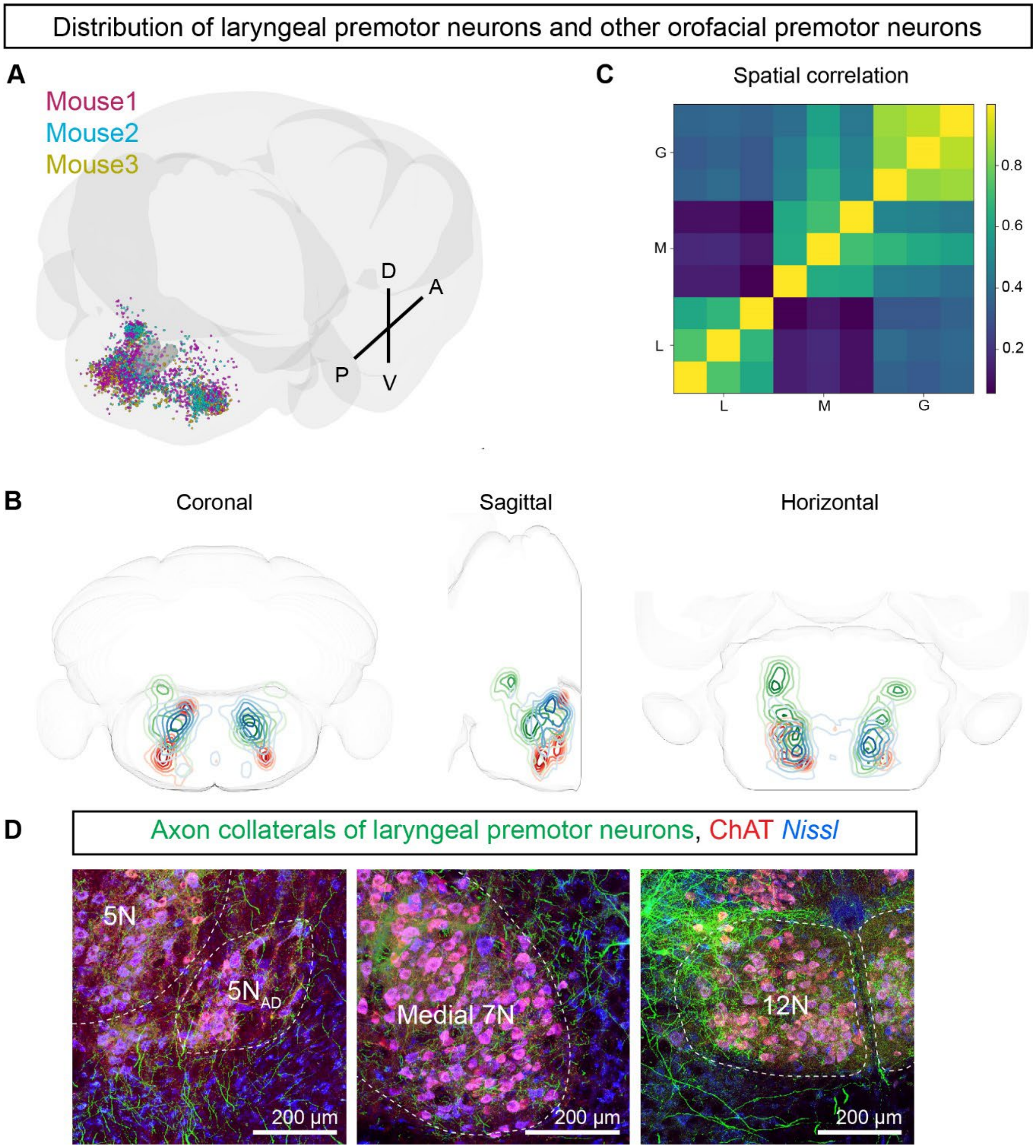

Fig. S1. Distribution of laryngeal premotor neurons and their collaterals to the other orofacial motor nuclei.

(A) 3D reconstructed distribution of laryngeal premotor neurons (magenta, aqua, and gold for 3 different mice) reconstructed in the CCF. (B) Spatial density distributions of the laryngeal premotor neurons (red) together with masseter (green) and genioglossus (blue) premotor neurons. (C) Cross-correlation of 3D spatial distributions of three orofacial premotor neurons (three examples for each: L (Larynx), M (Masseter), and G (Genioglossus). (D) Axon collaterals of rabies-labeled laryngeal premotor neurons (green) in other orofacial motor nuclei. The motor nuclei were revealed with ChAT immunolabeling (red). Neurotrace Blue was used to visualize neuronal structures. All scale bars indicate 200 µm.

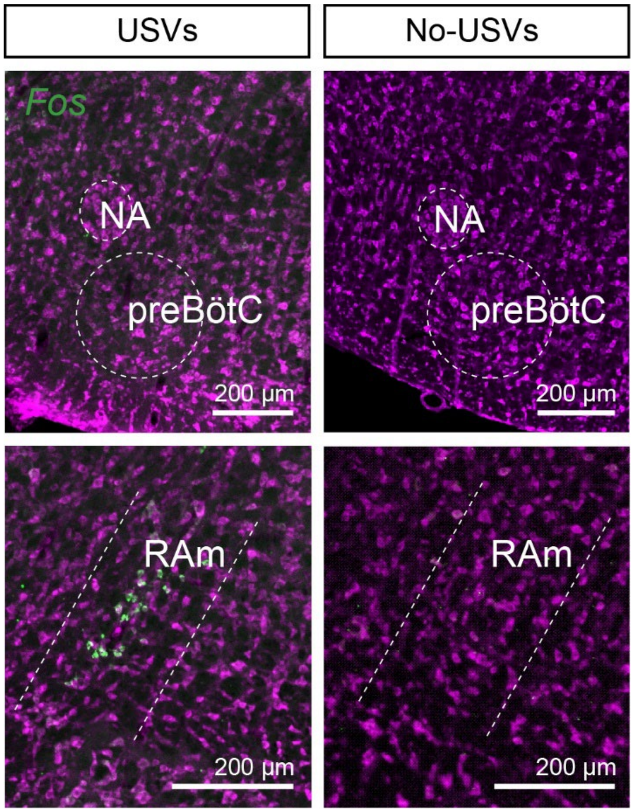

Fig. S2. Vocalization induced strong *Fos*+ expression in the RAm but not in the preBötC. Fluorescent in situ hybridization of *Fos* (green) in the preBötC (dash-circled, upper left) and RAm (bottom left) after female-directed male USVs. The right columns show *Fos* expression in the same regions without vocalization behaviors (male mice in a chamber alone). Note that no discernable *Fos* expression was found in the preBötC. Neurotrace Blue (magenta) was used to visualize neuronal structures. All scale bars indicate 200 µm.

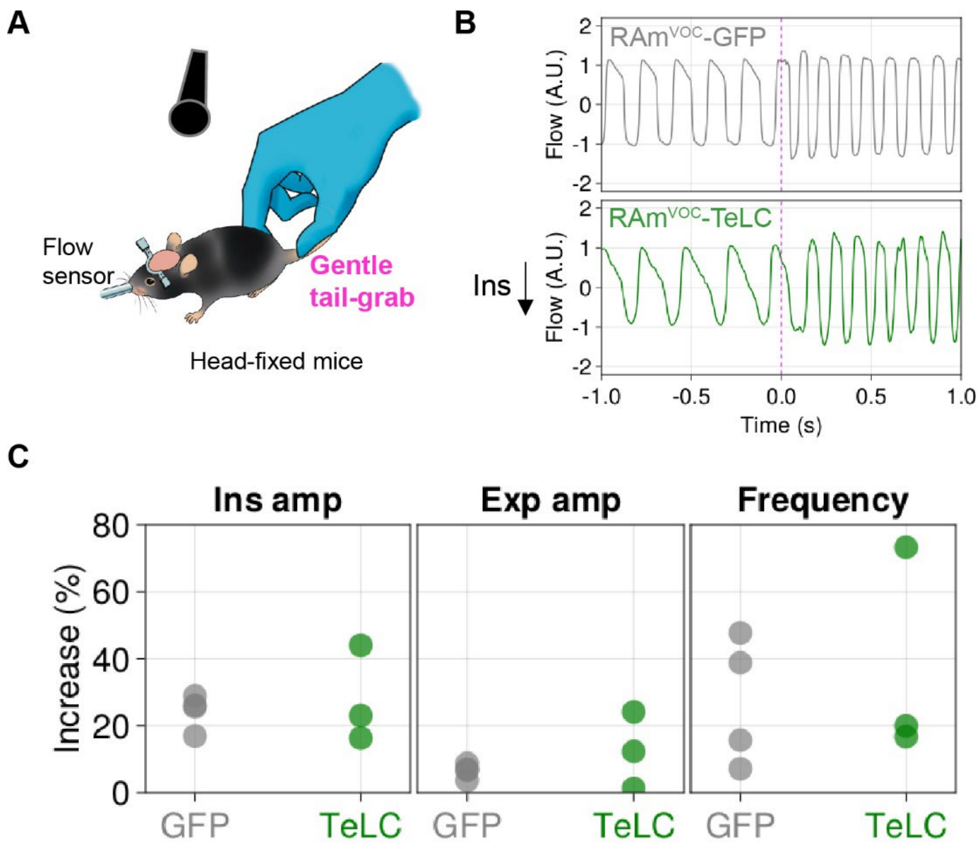

Fig. S3. RAm$^{\text{VOC}}$-TeLC mice were still able to modulate respiratory activity during running. (A) Schematic for encouraging mice to run for respiratory modulation. (B) Respiratory recordings in RAm$^{\text{VOC}}$-GFP (upper) and RAm$^{\text{VOC}}$-TeLC (bottom) mice. Magenta lines indicate the onsets of tail-grabbing. Note that downward flows correspond to inspirations. (C) Changes in inspiration (left) and expiration (middle) amplitude, and frequency (right) of respiratory flows. RAm$^{\text{VOC}}$-TeLC mice (green, n=3) and RAm$^{\text{VOC}}$-GFP control mice (grey, n=4)

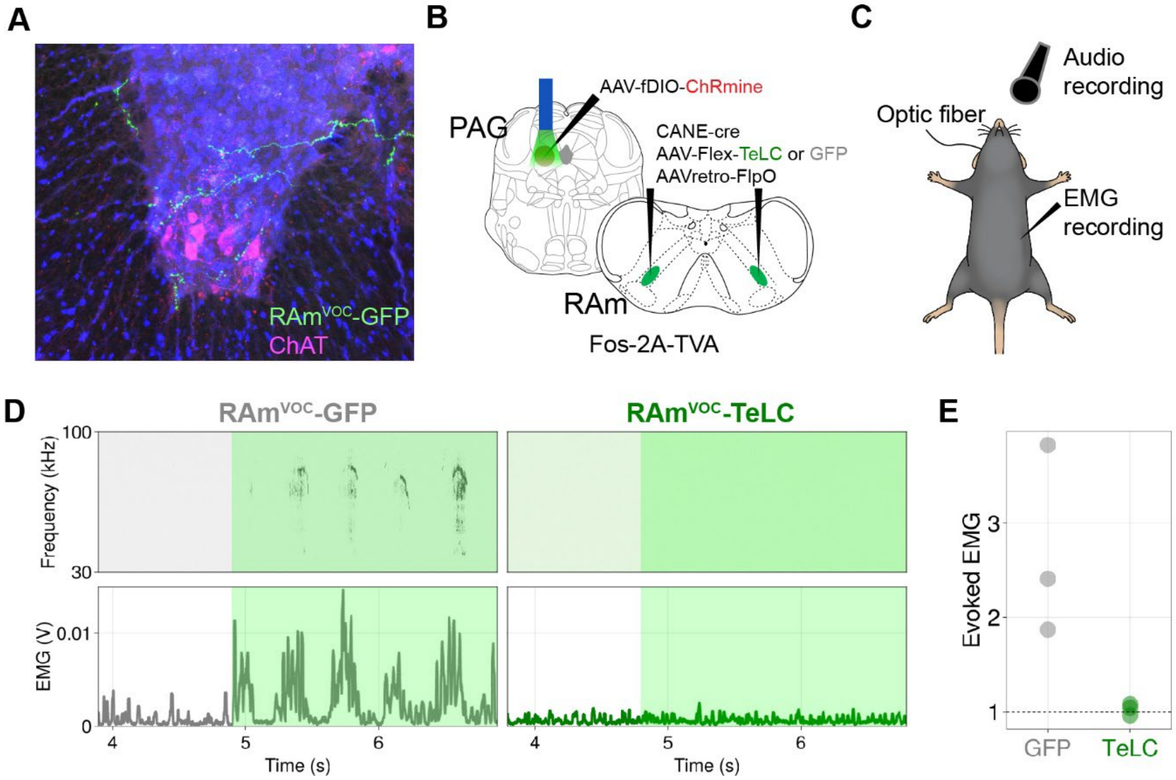

Fig. S4. PAG stimulation-evoked USVs and abdominal muscle activity were both abolished in RAm^{VOC}-TeLC mice.
(A) RAm^{VOC} axon terminals (GFP+) were observed in the thoracic spinal segment near motoneurons (ChAT+). (B) Schematic for eliciting USV in mice via PAG opto-stimulation. To target RAm projecting PAG neurons for vocalization, retrograde AAV-Flp and Flp dependent AAV- ChRmine were injected into the PAG and RAm, respectively. For RAm^{VOC} targeting, CANE-Cre and AAV-Flex-TeLC or GFP were injected into the RAm to express TeLC or GFP in RAm^{VOC}-neurons. (C) Sound and abdominal EMG recording during 2s PAG stimulation in anesthetized mice. (D) Spectrogram (upper) and EMG responses (RMS filtered, bottom) of GFP control and TeLC mice during PAG stimulation (2s, lime shades). (E) Evoked EMG responses (voltage) during PAG stimulation. RAm^{VOC}-TeLC mice (green, n=3) and RAm^{VOC}-GFP control mice (grey, n=3) Averaged EMG responses during PAG stimulation (2s) were normalized by averaged resting EMG responses (1s) to calculated PAG-evoked EMG.

Rabies labeled laryngeal premotor neurons in preBötC (RV-GFP) are *Vgat*+

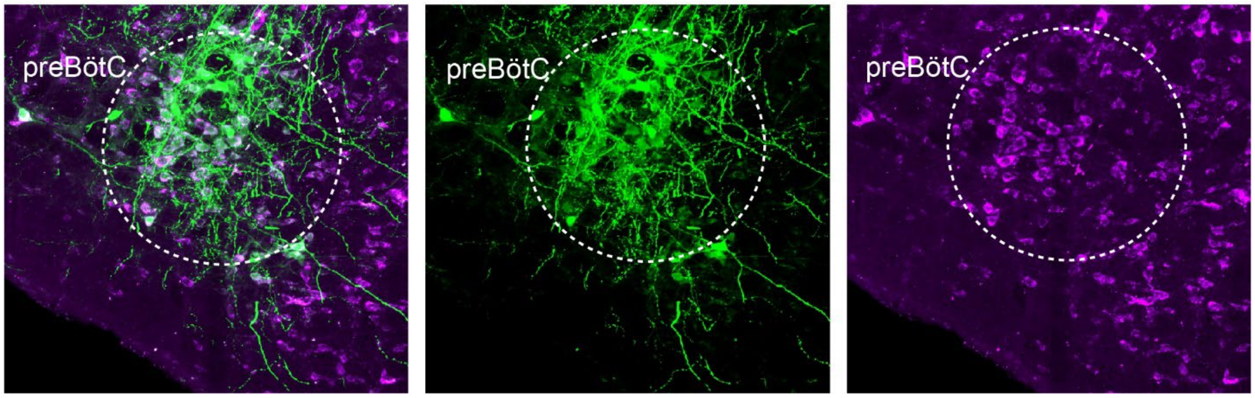

Fig. S5. preBötC contains *Vgat*+ inhibitory laryngeal premotor neurons.
Green neurons are laryngeal premotor neurons labeled with monosynaptic rabies-GFP through transsynaptic tracing (as described in Figure 1), and the in-situ hybridization signal with *Vgat* probe is shown in magenta.

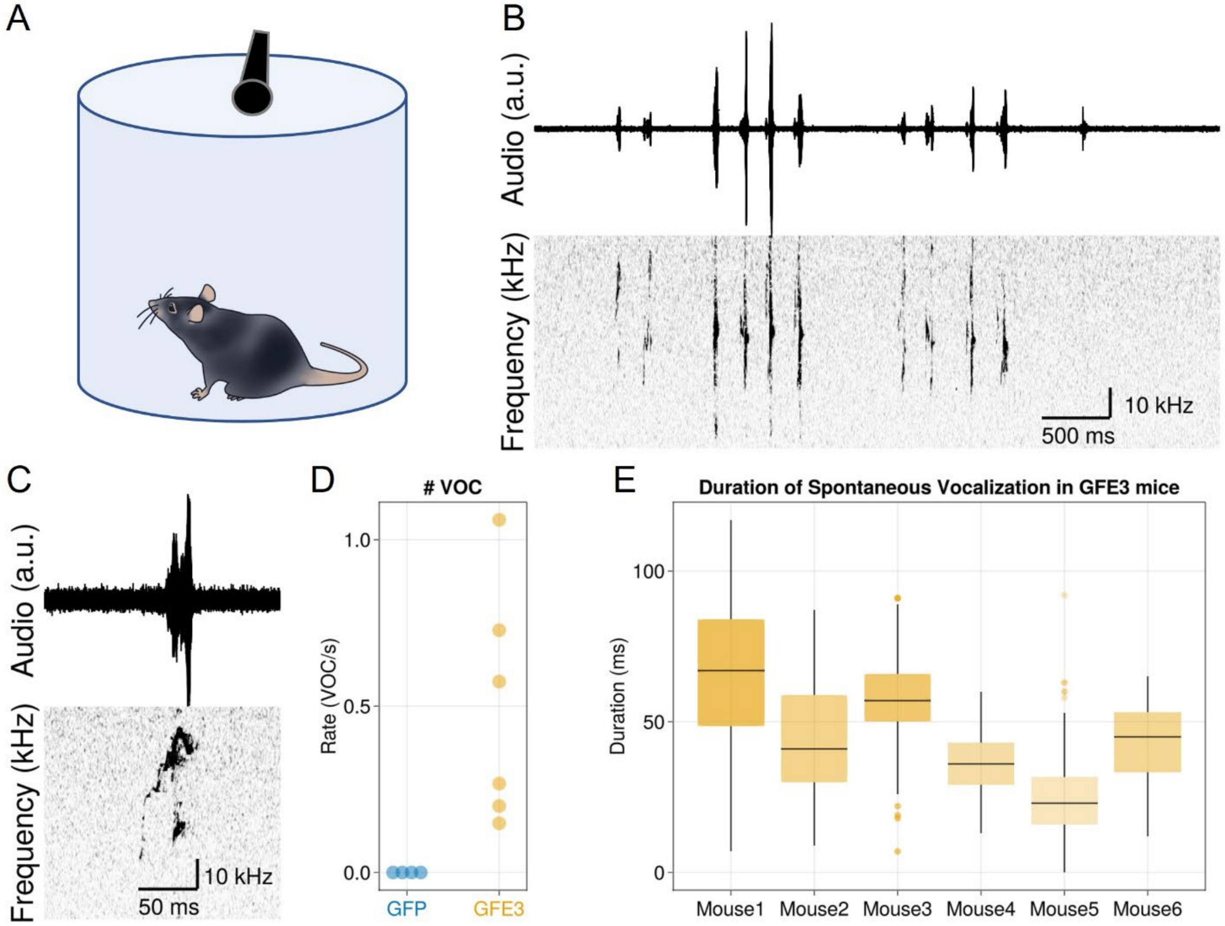

Fig. S6. Spontaneous vocalizations emerged in the RAm^{VOC}-GFE3 mice.
(A) Schematic for recording male mice vocalization in an isolation chamber. (B) Raw audio data (upper) and corresponding spectrogram plots (bottom). (C) An example of a single USV syllable from the spontaneous vocalizations. (D) Rates of spontaneous vocalizations in RAm^{VOC}-GFE3 mice (n=6) and RAm^{VOC}-GFP mice (n=4). Note that no spontaneous vocalization was found in the GFP control mice. (E) Durations of the spontaneous vocalizations of six RAm^{VOC}-GFE3 mice. Single dots show outliers.

Movie S1. A RAm^{VOC}-GFP mouse in a foot-shock chamber. Raw audio signals (upper left) and corresponding spectrogram (bottom left, in ultrasonic range). Sounds in the video (right) were recorded with an audible microphone.

Movie S2. A RAm^{VOC}-TeLC mouse in a foot-shock chamber. The mouse showed behavioral responses to foot-shock but did not produce audible squeaks.

Movie S3. Glottal responses to RAm^{VOC}-ChRmine stimulation. Four red dots are used to trace the glottal area. Red lines represent the glottal area. Green bars indicate the optogenetic stimulation periods.

References

45. F. Claudi *et al.*, Brainrender: a python-based software for visualizing anatomically registered data. *bioRxiv*, 2020.2002.2023.961748 (2020).
46. J. Takatoh *et al.*, The whisking oscillator circuit. *Nature* **609**, 560-568 (2022).
47. T. Nath *et al.*, Using DeepLabCut for 3D markerless pose estimation across species and behaviors. *Nature Protocols* **14**, 2152-2176 (2019).